Research Square

Preprints are preliminary reports that have not undergone peer review.
They should not be considered conclusive, used to inform clinical practice,
or referenced by the media as validated information.

Gut microbiota-derived butyrate ameliorates pediatric IgA vasculitis via GPR43 by inhibiting the NF-κB/NLRP3 inflammatory cascade and attenuating Tfh17-driven IgA production

Yujing Gu
Ningxia Medical University General Hospital
Xiaolong Ma
Ningxia Medical University
Jiahui Wang
Ningxia Chinese Medicine Research Center
Ting Ma
Ningxia Medical University
Zhijia Yan
Ningxia Medical University
Jinhai Ma
Ningxia Medical University General Hospital
Xiaoxia Zhang
Ningxia Medical University
Hao Wang
wanghaograduate@126.com

Ningxia Medical University

Article

Keywords: IgAV, Butyrate-producing gut microbiota, Clostridium butyricum, Butyrate, GPR43, Tfh 17 cell differentiation

Posted Date: November 18th, 2026

DOI: https://doi.org/10.21203/rs.3.rs-11101186/v1

License: This work is licensed under a Creative Commons Attribution 4.0 International License.
Read Full License

Additional Declarations: No competing interests reported.

Gut microbiota-derived butyrate ameliorates pediatric IgA vasculitis via GPR43 by inhibiting the NF-κB/NLRP3 inflammatory cascade and attenuating Tfh17-driven IgA production

Yujing Gu[1], Xiaolong Ma[2], Jiahui Wang[3], Ting Ma[2], Zhijia Yan[2], Jinhai Ma[1*], Xiaoxia Zhang[4*], Hao Wang[2*]

[1]Department of Pediatrics, General Hospital of Ningxia Medical University, Yinchuan 750004, Ningxia, China;

[2]Ningxia Key Laboratory of Infection and Immunity, School of Basic Medical Sciences, Ningxia Medical University, Yinchuan 750004, Ningxia, China;

[3]Department of Nephrology, Ningxia Chinese Medicine Research Center, Yinchuan 750021, Ningxia, China;

[4]School of Traditional Chinese Medicine, Ningxia Medical University, Yinchuan 750004, Ningxia, China.

EMails: Yujing Gu, 18809600732@163.com; Xiaolong Ma, m15109585482@126.com; Jiahui Wang, 398932672@qq.com; Ting Ma, 1127970397@qq.com; Zhijia Yan, 1015460050@qq.com; Jinhai Ma, makhcn@163.com; Xiaoxia Zhang, zxx1216@163.com; Hao Wang, wanghaograduate@126.com.

Corresponding authors

*Hao Wang, Ningxia Key Laboratory of Infection and Immunity, School of Basic Medical Sciences, Ningxia Medical University, Yinchuan, Ningxia, China; Email: wanghaograduate@126.com. Primary correspondence and proofs: Hao Wang.

*Xiaoxia Zhang, School of Traditional Chinese Medicine, Ningxia Medical University, Yinchuan, Ningxia, China; Email: zxx1216@163.com.

*Jinhai Ma, Department of Pediatrics, General Hospital of Ningxia Medical University, Yinchuan, Ningxia, China; Email: makhcn@163.com.

Abstract

Immunoglobulin A vasculitis (IgAV) is the most common pediatric systemic small-vessel vasculitis, with renal involvement directly determining long-term prognosis; yet no etiology-targeted interventions are clinically available. Butyrate, a gut microbiota-derived metabolite that regulates mucosal immune homeostasis, has unclear mechanisms underlying its effects on IgAV-associated multiorgan damage. Here we show that butyrate-producing microbiota are specifically depleted in children with active IgAV. Among seven major short-chain fatty acids, only butyrate is significantly decreased and tends to be negatively correlated with disease activity and renal injury indices. Using an ovalbumin-induced IgAV rat model, we demonstrate that sodium butyrate and *Clostridium butyricum* both reduce IgA immune complex deposition and multi-organ inflammatory infiltration via GPR43, synergistically repairing the intestinal barrier, suppressing NF-κB/NLRP3 activation and IL-6/STAT3-dependent Tfh17 differentiation, and inhibiting aberrant IgA production. These findings reveal a gut dysbiosis – butyrate deficiency – IgAV pathogenesis cascade, supporting butyrate-based preparations as a promising etiology-targeted intervention for IgAV.

Keywords IgAV, Butyrate-producing gut microbiota, *Clostridium butyricum*, Butyrate, GPR43, Tfh 17 cell differentiation

1. Introduction

The gut microbiota and its metabolites represent an important class of microecological regulatory factors in autoimmune diseases[1–3]. The gut microbiome is often referred to as the host's "second genome"[4], and its metabolites participate in maintaining the intestinal barrier, shaping immune homeostasis, and regulating systemic physiological functions through cross-interface signaling[5]. Disruptions in microbial composition and metabolic function can compromise the mucosal barrier and disrupt immune tolerance, and are recognized as key drivers of the onset and progression of various immune-related diseases[6]. Short-chain fatty acids (SCFAs) are the primary metabolites produced by the gut microbiota via dietary fiber fermentation, and mainly include acetic acid, propionic acid, and butyric acid. Among these, butyric acid not only provides energy to colonic epithelial cells but also mediates interactions between the microbiota and the immune system[7]. Previous studies have shown that SCFAs can regulate the differentiation and function of T cells, B cells, and myeloid cells, and are involved in establishing immune tolerance and maintaining inflammatory homeostasis[8,9]; however, the specific molecular mechanisms by which SCFAs regulate the abnormal differentiation of immune cell subsets and mediate the spread of mucosal immune dysregulation to the systemic level in the context of specific diseases remain unclear.

Immunoglobulin A vasculitis (IgAV) is the most common systemic small-vessel vasculitis in childhood. Its core pathological feature is the deposition of IgA-predominant immune complexes in the walls of small blood vessels throughout the body. The annual incidence of IgAV in children is approximately 20 per 100,000. The course of the disease is self-limiting in most children, but 20%–54% may progress to IgAV-associated nephritis, and 1%–7% eventually progress to chronic kidney disease or even end-stage renal disease[10,11]. The classic "multiple-hit" theory has elucidated the pathological cascade involving the production of galactose-deficient IgA1 (Gd-IgA1),

immune complex deposition, and downstream inflammatory damage[12]. However, the upstream initiating factors leading to the persistent abnormal production of pathogenic IgA1 remain unclear, and there remains a lack of precise clinical intervention strategies based on the microbiome–immune axis.

Recent clinical cohort studies have shown that the abundance of butyrate-producing bacteria, such as *Roseburia* and *Faecalibacterium*, is specifically reduced in the intestines of children with IgAV and is negatively correlated with disease severity[13,14]. However, these studies have largely remained at the level of descriptive analysis of microbial species composition and have not yet identified the downstream effector molecules and regulatory pathways through which they mediate immune damage.

The abnormal production and deposition of pathogenic IgA represent the central initiating event in the pathogenesis of IgAV. Traditional studies have largely focused on endogenous glycosylation defects in B cells[15]. However, accumulating evidence has been confirming that co-stimulatory signals provided by $CD4^+$ follicular helper T cells serve as upstream drivers governing B-cell activation and pathogenic antibody class switching[16,17]. T follicular helper 17 (Tfh17) is a functional subset that co-expresses the transcription factors Bcl-6 and RORγt, integrating germinal center B-cell helper activity with Th17-type proinflammatory properties. Mechanistically, Tfh17 secretes IL-21 to support B-cell IgA production and affinity maturation, and concurrently drives the formation of a local proinflammatory microenvironment via IL-17, thereby jointly modulating the IgA immune response[18,19]. Clinical studies have verified that the frequency of circulating $CD4^+CXCR5^+CCR6^+$ Tfh17 cells is significantly increased in patients with IgAV, and positively correlates with serum Gd-IgA1 levels, disease

severity, and the degree of renal injury[20]. Existing evidence indicates that the IL-6/STAT3 signaling axis is one of the core pathways governing Tfh17 cell differentiation. IL-6 activates the STAT3 transcription factor to promote the polarization of naive T cells toward the Tfh17 lineage[21,22]. Whether gut microbiota-derived metabolites mediate the pathological expansion of Tfh17 cells by modulating this pathway in IgAV remains to be systematically elucidated.

As core metabolites of the gut microbiota, SCFAs exert their biological effects primarily via membrane receptors[23]. G protein-coupled receptor 43 (GPR43), also termed free fatty acid receptor 2 (FFAR2), is a specific membrane receptor for SCFAs. It is widely expressed on intestinal mucosal epithelial cells and multiple immune cell subsets[24], and mediates transmucosal transduction of microbial metabolic signals[25]. GPR43 is involved in SCFA-mediated regulation of systemic immune-inflammatory responses and $CD4^+$ T-cell subset homeostasis, and exerts protective effects in multiple autoimmune disease models[26]. Collectively, whether butyrate can inhibit the IL-6/STAT3 pathway via GPR43, thereby reducing pathological Tfh17 cell expansion and alleviating IgAV-associated immune damage, remains to be validated by systematic *in vitro* and *in vivo* experiments.

Based on the aforementioned research background, this study proposes the following scientific hypothesis: butyrate deficiency resulting from the depletion of butyrate-producing bacteria is an upstream driving event of intestinal immune homeostasis disruption in IgAV; butyrate maintains intestinal mucosal barrier function, at least in part, by activating the GPR43 receptor, thereby inhibiting the excessive expansion of Tfh17 cells and aberrant production of pathogenic IgA, ultimately alleviating multisystem immune injury. Using a combination of clinical multi-omics

119 analysis, intervention in an ovalbumin (OVA)-induced IgAV rat model, and molecular
120 mechanism validation, this study systematically investigates the protective role and
121 regulatory pathways of the butyrate-producing bacteria–butyrate–GPR43 axis in IgAV.
122 From the perspective of microbial metabolism, this work delineates the regulatory
123 mechanisms underlying the upstream initiating events of IgAV, and provides novel
124 insights and a theoretical foundation for microbiome-based interventions for the
125 disease.

126 ## 2. Results

127 ### 2.1 Disruption of Gut Microbiota Structure and Depletion of Butyrate-Producing
128 Bacteria in Patients with IgAV

129 To characterize gut microbiota dysbiosis in patients with IgAV, this study employed
130 metagenomic sequencing to analyze differences in species composition and gene
131 profiles of fecal microbiota between 25 IgAV patients and 25 age- and sex-matched
132 healthy controls. Alpha diversity analysis revealed that the Shannon index of the gut
133 microbiota in IgAV patients showed a downward trend, accompanied by increased
134 intra-group dispersion (Figure 1A). Unsupervised principal coordinate analysis (PCoA)
135 based on Bray-Curtis distance demonstrated a clear separation of the overall gut
136 microbiota community structure between the two groups (Figure 1B), indicating
137 significant disruption of gut microbiota structure in IgAV patients. Venn analysis at the
138 gene set level revealed that the two groups shared 1,585,246 core microbial genes;
139 while healthy controls and patients harbored 1,786,167 and 1,830,778 unique genes,
140 respectively, suggesting remodeling of the gut microbial gene profile under disease
141 conditions (Figure 1C).

Taxonomic annotation results showed that, at the phylum level, both groups were dominated by Bacillota and Bacteroidota, which together accounted for more than 90% of the total abundance (Figure 1D). Compared to healthy controls, IgAV patients exhibited a significantly reduced abundance of Bacillota ($P < 0.01$) and a significantly increased abundance of Bacteroidota ($P < 0.05$); the Bacillota/Bacteroidota ratio was also significantly decreased ($P < 0.05$), suggesting phylum-level microbiota dysbiosis in patients (Figure 1G). The genus-level community composition was consistent with the phylum-level trend: core dominant genera in both groups included *Parabacteroides*, *Bacteroides*, *Roseburia*, and *Faecalibacterium*; in the IgAV group, the overall proportion of commensal genera within Bacillota was reduced, while that of genera within Bacteroidota was correspondingly expanded (Figure 1E). Differential abundance analysis showed that core butyrate-producing genera such as *Butyricicoccus*, *Eubacterium*, and *Roseburia*, as well as functional commensal genera of Bacillota such as *Clostridium*, were all significantly depleted in patients (all $P < 0.05$; Figure 1H). Results at the species level further corroborated the depletion of butyrate-producing bacteria: the overall proportion of butyrate-producing species in the IgAV group was decreased, while the proportion of commensal species in Bacteroidota was increased (Figure 1F); among these, the abundance of key potent butyrate-producing species such as *Roseburia hominis* and *Roseburia intestinalis* was significantly reduced (all $P < 0.05$; Figure 1I). In summary, widespread depletion of functional butyrate-producing bacterial communities is a core feature of gut dysbiosis in patients with IgAV.

2.2 Alterations in Microbial Functional Profile, Specific Reduction of Butyrate, and Correlations with Clinical Indicators

Building on the identified species-level dysbiosis, we further validated changes in the butyrate-producing capacity of gut microbiota through functional profile annotation and metabolite quantification, and analyzed its correlation with clinical indicators. Functional profiling based on KEGG database annotation revealed distinct differentiation of gut microbial functional profiles between the two groups; the first two principal components collectively explained 76.38% of the functional variation (Figure 2A). At the KEGG pathway level, the profiles were dominated by basic functions such as ABC transporters, ribosome, and carbohydrate metabolism, and the overall functional profile showed a disease-specific shift (Figure 2B). Differential abundance analysis of pathways showed that the butyrate metabolism pathway trended toward decreased abundance in IgAV patients, meanwhile other abundances of starch and sucrose metabolism and glycerolipid metabolism pathways were significantly reduced ($P < 0.05$, Figure 2C). To further delineate the molecular basis underlying this trend, we quantified two key terminal enzymes mediating butyrate biosynthesis: butyrate-CoA transferase was significantly decreased in IgAV patients ($P < 0.05$), while butyrate kinase showed a consistent downward trend (Figure 2D). The attenuated carbohydrate metabolic potential and reduced butyrate biosynthetic capacity at both the pathway and functional gene levels were concordant with the species-level depletion of butyrate-producing bacteria. Quantitative detection of seven fecal SCFAs showed no statistically significant differences in the levels of acetic acid, propionic acid, isobutyric acid, valeric acid, isovaleric acid, and caproic acid between the two groups (all $P > 0.05$). Only butyrate was significantly decreased in IgAV patients ($P < 0.05$, Figure 2E), indicating that the abnormality of gut SCFAs in IgAV patients is mainly characterized by a specific reduction of butyrate.

Clinical baseline data showed that in the overall cohort of 117 patients with active IgAV, the levels of 24-hour urinary protein (24h UP, $P < 0.01$), plasma IgA ($P < 0.001$), IL-6 ($P < 0.01$), CRP ($P < 0.05$), and ESR ($P < 0.01$) differed significantly from the laboratory upper limit of normal (ULN). FIB levels showed no statistically significant deviation from the normal reference range ($P > 0.05$, Figure 2F), indicating the presence of systemic inflammation and renal impairment in this IgAV cohort. Subgroup analysis stratified by IgAVN showed that plasma levels of IgA, IL-6 and CRP were significantly higher in IgAVN patients than in non-renal IgAV patients (all $P < 0.05$, Figure 2G). In the omics subcohort, Spearman's rank correlation analysis revealed a trend toward negative correlations between fecal butyrate levels and IL-6, plasma IgA, and 24h UP, respectively (Figure 2H). Correlation analysis of microbiota, pathways, and clinical indicators showed that five butyrate-producing genera were positively correlated with both butyrate metabolism and starch and sucrose metabolism pathways; among them, *Roseburia* was significantly positively correlated with the butyrate metabolism pathway (Figure 2I). Regarding clinical correlations, the abundance of butyrate-producing bacteria was generally negatively correlated with IgA, inflammation, and markers of renal injury. Specifically, *Roseburia* was significantly negatively correlated with plasma CRP ($P < 0.01$, Figure 2J), supporting the close association between butyrate-producing bacteria and humoral immune disorders as well as inflammatory status in IgAV.

2.3 *C. butyricum* and NaB Improve Disease Phenotype and Renal Function in IgAV Rats

Based on the findings from the clinical cohort that gut butyrate-producing bacteria were depleted and butyrate levels were decreased in IgAV patients, this study further

validated the interventional effects of butyrate in an animal model. The IgAV model was established in SD rats via induction with OVA combined with CFA. Rats were administered *C. butyricum* or NaB at different doses (500, 1000 mg/kg), respectively. The timeline of model establishment and the intervention protocol are shown in Figure 3A. Dynamic monitoring of body weight showed no statistically significant difference in baseline body weight among all groups, and body weight increased naturally over the experimental period in all groups. Compared to the CON group, the rate of body weight gain in the IgAV model group was significantly attenuated. After intervention with *C. butyricum* or NaB, the rate of body weight gain recovered to varying degrees (Figure 3B). Macroscopic observation of the skin revealed multiple petechiae and purpura-like erythema on the tail and back of rats in the model group, which was consistent with the characteristic manifestations of IgAV-associated cutaneous small-vessel vasculitis. In each intervention group, the extent of cutaneous purpura was reduced and the severity of lesions was alleviated, with a more pronounced ameliorative effect observed in the high-dose NaB group (Figure 3C-D).

In IgAV, the kidney is the key visceral target organ that determines long-term prognosis. This study evaluated the degree of renal damage from three dimensions: filtration function, urinary sediment, and barrier integrity. Compared with the CON group, the model group exacerbated levels of SCr, UUN, URBC, UTP, and UPCR along with decreased UCr levels (Figure 3E–H), suggesting impaired glomerular filtration function and disrupted integrity of the filtration barrier. After intervention with *C. butyricum* or NaB, all aforementioned renal parameters were ameliorated to differing extents, among which proteinuria and hematuria were significantly improved, indicating that butyrate intervention can effectively alleviate renal damage in the IgAV model.

2.4 *C. butyricum* and NaB Alleviate Pathological Damage of Cutaneous and Renal Small-Vessel Vasculitis

Building on the ameliorative effects of butyrate on disease phenotype and renal function in IgAV rats, this study further evaluated the severity of small-vessel vasculitis in the skin and kidney, as well as the deposition levels of IgA and complement C3, via histopathological staining and immunolabeling techniques.

HE staining of skin sections showed that in the CON group, the structure of dermal small vessels was intact, with no obvious perivascular inflammatory cell infiltration. In the IgAV model group, fibrinoid necrosis was observed in the walls of dermal small vessels, accompanied by perivascular infiltration of neutrophils and lymphocytes with karyorrhexis and erythrocyte extravasation, which was consistent with the typical pathological features of leukocytoclastic vasculitis. After intervention with *C. butyricum* and various doses of NaB, the scope of vascular wall necrosis was reduced, and the surrounding inflammatory infiltration was alleviated with variable efficacy across groups (Figure 4A). Quantitative results of IF and IHC showed that the deposition levels of IgA and C3 in the dermal small vessel walls were significantly elevated in the model group, and the two colocalized in the vascular wall region. In all intervention groups, the levels of both were concordantly decreased, and the ameliorative effect of NaB showed a dose-dependent trend (Figure 4B-C, H-I). The results indicate that butyrate can alleviate pathological damage of cutaneous small vessels in IgAV rats, and this effect is accompanied by reduced deposition of IgA immune complexes and complement C3 in the vascular walls.

Renal pathological results showed that in the CON group, glomerular and tubular structures were clear, with no abnormal proliferation in the mesangial region. In the

model group, glomerular volume was enlarged, with diffuse proliferation of mesangial cells and matrix; PAS staining confirmed excessive deposition of mesangial matrix, accompanied by tubular epithelial degeneration, protein cast formation and renal interstitial inflammatory infiltration, which was consistent with the pathological manifestations of mesangial proliferative purpuric nephritis. After butyrate intervention, glomerular mesangial proliferation was reduced, and overall renal pathological damage was alleviated (Figure 4D-E). Co-deposition of IgA and C3 was observed in the glomerular mesangial region; the levels of both in the model group were significantly higher than those in the control group, and they decreased concordantly after butyrate intervention, with the change trend highly consistent with the improvement of renal pathology (Figure 4F-G, J-K), suggesting that butyrate can also alleviate renal pathological damage in IgAV rats.

2.5 *C. butyricum* and NaB Alleviate Intestinal Small-Vessel Vasculitis Damage and Restore the Intestinal Barrier

In addition to the skin and kidneys, the intestine is also a common target organ affected by IgAV, and endotoxin translocation mediated by intestinal barrier damage is a key link in amplifying systemic inflammation. This study further examined intestinal pathological changes and evaluated intestinal barrier function from multiple dimensions, including the physical barrier, mucus barrier, and endotoxin translocation.

HE staining of colonic sections showed that in the CON group, the colonic mucosal structure was intact, with well-organized crypts and a continuous epithelial layer; in the model group, crypt structures were disorganized, with epithelial necrosis and desquamation, and inflammatory cell infiltration in the lamina propria and submucosa accompanied by vascular congestion, consistent with the manifestations of

intestinal small-vessel vasculitis. After butyrate intervention, pathological damage to the colonic mucosa was reduced to different levels (Figure 5A). Changes in IgA and C3 deposition in the small intestinal mucosa followed similar trends to those observed in the skin and kidneys: levels of both were significantly elevated in the model group and decreased following a series of butyrate intervention (Figure 5B–E), suggesting that butyrate can alleviate vasculitic damage in multiple intestinal segments in IgAV rats.

Assessment of intestinal barrier function showed that in the CON group, the intestinal epithelial tight junction protein ZO-1 exhibited a continuous linear distribution, and goblet cell mucin MUC2 was abundantly expressed, suggesting structural integrity of both the physical and mucus barriers. In the model group, ZO-1 distribution was disrupted and fluorescence intensity was reduced, with a concurrent decrease in MUC2 expression, indicating that both layers of the intestinal barrier were compromised (Figure 5F-G). Quantitative analysis showed that the relative fluorescence intensities of both ZO-1 and MUC2 in the model group were significantly lower than those in the control group; following butyrate intervention, the expression of both barrier proteins was restored in a group-specific manner (Figure 5I-J). Ki-67 IHC showed that the proportion of Ki-67-positive cells in the intestinal crypt region of the model group was significantly elevated, suggesting increased proliferative activity of the intestinal epithelium under pathological conditions; following butyrate intervention, the positive proportion decreased, reflecting alleviated epithelial damage and gradual restoration of proliferative homeostasis (Figure 5H, K). Plasma LPS measurement showed that plasma LPS levels were significantly elevated in the model group, suggesting endotoxin translocation caused by increased intestinal barrier permeability; plasma LPS levels in all butyrate intervention groups were lower than

312 those in the model group, consistent with the improvement of intestinal barrier function
313 (Figure 5L).

314 **2.6 *C. butyricum* and NaB Ameliorate Circulating and Local Renal Inflammatory**
315 **Factor Imbalance and Regulate the GPR43/NF-κB/NLRP3 Pathway**

316 Intestinal barrier damage can lead to endotoxin translocation and subsequent systemic
317 inflammation. Building on the aforementioned improvement of intestinal barrier
318 function, this study further detected the expression levels of inflammatory factors in
319 plasma and renal tissue, and assessed the expression changes of key molecules in the
320 GPR43/NF-κB/NLRP3 inflammatory pathway at both the transcriptional and protein
321 levels, to explore the potential molecular mechanisms underlying the anti-inflammatory
322 effect of butyrate.

323 Measurement of plasma inflammatory factors showed that both pro-inflammatory
324 and anti-inflammatory factors in the CON group were at baseline levels. In the IgAV
325 model group, the levels of TNF-α, IL-6, IL-1β and IL-18 were significantly elevated,
326 while the level of the anti-inflammatory factor IL-10 was significantly decreased,
327 suggesting a systemic inflammatory factor imbalance (Figures 6A–C, S1A–B). After
328 intervention with *C. butyricum* and various doses of NaB, the aforementioned pro-
329 inflammatory factors exhibited divergent reduction trends, and IL-10 levels showed a
330 trend of recovery. The changes of inflammatory factors in renal tissue were highly
331 consistent with the plasma trends: in the model group, the expression of pro-
332 inflammatory factors in renal tissue was significantly upregulated and IL-10 expression
333 was downregulated; butyrate intervention ameliorated the local renal inflammatory
334 factor imbalance, with improvement patterns varying across intervention groups
335 (Figures 6D–F, S1C–D). The results indicate that butyrate can simultaneously

ameliorate the inflammatory factor imbalance in both the circulation and local renal tissue of IgAV rats.

qPCR results showed that compared with the CON group, the mRNA expression of *Ffar2* in renal tissues of the IgAV model group was significantly downregulated, while the mRNA levels of *Rela*, *Nlrp3* and their downstream pro-inflammatory cytokine genes were all significantly elevated. After butyrate intervention, the above transcriptional abnormalities were unevenly reversed, and the regulatory effect of NaB showed a dose-dependent trend (Figures 6G–I, S1E–H). Western blot validation results were consistent with the transcriptional changes: in the model group, the protein level of GPR43 in renal tissue was decreased, the level of phosphorylated NF-κB p65 (p-p65) was increased, and the protein levels of core components of the NLRP3 inflammasome (NLRP3, ASC, Pro-caspase-1) and the downstream effector molecule IL-6 were all upregulated. After butyrate intervention, the aberrant expression of these pathway proteins exhibited distinct reversal patterns, suggesting that butyrate may participate in the regulation of renal inflammation by restoring GPR43 expression and inhibiting the activation of the NF-κB/NLRP3 inflammatory pathway (Figure 6J–P).

2.7 *C. butyricum* and NaB Regulate the IL-6/STAT3-Tfh17 Axis and IgA Response

Based on the marked downregulatory effect of butyrate on the renal pro-inflammatory factor IL-6, this study further analyzed the activation status of the renal IL-6/STAT3 pathway, the proportion of Tfh17 cells in multiple immune organs, and the IgA response level, to investigate the regulatory effect of butyrate on adaptive immune dysregulation.

qPCR results showed that *Stat3* mRNA expression in renal tissues of the IgAV model group was significantly upregulated. The mRNA levels of Tfh17-associated

transcription factors *Rorc* and *Bcl6*, the chemokine receptor *Cxcr5*, and downstream effector cytokines *Il17a* and *Il21* were all significantly elevated, suggesting activation of the STAT3 pathway and abnormal transcriptional upregulation of Tfh17-associated molecules. Following intervention with *C. butyricum* or NaB, the abnormal transcription of the aforementioned genes exhibited graded reversal, and the regulatory effect of NaB displayed a dose-dependent trend (Figure 7A–F). Western blot analysis further validated the activation status of the STAT3 pathway: total STAT3 protein levels in renal tissue showed no significant difference among all groups; the IgAV model group exhibited significantly elevated levels of phosphorylated STAT3 (p-STAT3), suggesting that the abnormal activation of the STAT3 pathway mainly occurred at the level of phosphorylation modification rather than upregulation of total protein expression. Following butyrate intervention, p-STAT3 protein levels showed differential downregulation across groups, consistent with the trends observed at the transcriptional levels (Figure 7G–H).

Flow cytometry was used to detect cell subsets in mesenteric lymph nodes (MLNs), spleen, and peripheral blood. The results showed that compared with the CON group, the proportion of Tfh17 cells in the MLNs, spleen, and peripheral blood of the IgAV model group was significantly increased, and the proportion of IgA^+ B cells was concurrently increased. Following intervention with *C. butyricum* or NaB, the proportions of both cell subsets were reduced to disparate degrees, and the regulatory effect of NaB exhibited a dose-dependent trend (Figure 8A–F). Spearman correlation analysis showed that the proportion of Tfh17 cells was significantly positively correlated with the proportion of IgA^+ B cells in the MLNs, spleen, and peripheral blood, suggesting that the increased proportion of Tfh17 cells may promote B cell differentiation into the IgA subtype via helper function (Figure 8G). ELISA

quantification results were consistent with the changes in cell phenotypes: in the IgAV model group, levels of IL-21, the characteristic effector cytokine of Tfh17 cells, were significantly elevated in both plasma and renal tissue, along with a concurrent increase in plasma IgA concentration. Following butyrate intervention, all these indicators exhibited a spectrum of reduction amplitudes, consistent with the trends of cell proportions and upstream pathway molecules (Figure 8H–J).

2.8 *C. butyricum* and NaB Regulate Gut Microbiota Diversity and Community Composition in IgAV Rats

The above results indicate that butyrate may exert multi-organ protective effects by inhibiting the GPR43/NF-κB/NLRP3 inflammatory pathway and regulating the IL-6/STAT3-Tfh17 immune axis. Given that the primary site of butyrate action is the intestine, and that the gut microbiota is both the source of butyrate and a target of its regulation, this study further employed 16S rRNA high-throughput sequencing to analyze changes in the diversity and species composition of rat fecal microbiota after butyrate intervention, to explore the association between microbiota remodeling and the ameliorative effects of butyrate on IgAV.

Rarefaction curves showed that the curves for samples in each group gradually plateaued with increasing sequencing depth, indicating that the sequencing data volume was sufficient to stably reflect the microbial composition of the samples (Figure 9A). Alpha diversity analysis revealed significant differences in the ACE index of gut microbiota among groups (Kruskal-Wallis test). Compared with the CON group, the microbial species richness of the IgAV model group was significantly increased. After intervention with *C. butyricum* or NaB, microbial richness shifted in a group-dependent manner (Figure 9B). PCoA of Beta diversity based on Bray-Curtis distance showed that

409 the microbial community structures of all groups were clearly distinguishable
410 (PERMANOVA, $R = 0.7755$, $P = 0.001$); samples from the CON group and the IgAV
411 model group were completely separated in clustering, while samples from the butyrate
412 intervention groups showed a relatively independent distribution (Figure 9C).
413 Intergroup Beta diversity distance analysis showed significant differences in the degree
414 of community dispersion among groups (Wilcoxon rank-sum test); the intra-group
415 dispersion of the model group was higher than that of the control group, and butyrate
416 intervention modulated dispersion levels with distinct patterns across groups (Figure
417 9D). Petal plot analysis revealed that the eight groups shared a total of 34 core ASVs;
418 the number of unique ASVs in the model group was higher than that in the control
419 group, and the number of unique ASVs further increased after butyrate intervention
420 (Figure 9E).

421 Species composition analysis showed intergroup differences in gut microbiota at
422 three taxonomic levels: phylum, genus, and species. At the phylum level, Bacillota and
423 Bacteroidota were the dominant phyla in all groups. Compared with the CON group,
424 the IgAV model group showed increased abundance of Bacillota and decreased
425 abundance of Bacteroidota; these compositional shifts exhibited a range of reversal
426 magnitudes after intervention with *C. butyricum* or NaB (Figure 9F). At the genus level,
427 the IgAV model group had lower abundances of beneficial genera such as *Duncaniella*
428 and *Romboutsia*, and higher abundances of taxonomic units such as
429 *norank_f__Prevotellaceae* and *norank_f__Oscillospiraceae* (Figure 9G). The trends at
430 the species level were consistent with those at the genus level (Figure 9H): the
431 abundance of *Ligilactobacillus animalis* was significantly downregulated in the model
432 group, while *Prevotellaceae*-related species were significantly enriched.

2.9 Screening of Differential Microbiota and Correlation Analysis with IgAV Pathological Indicators

To identify the specific taxonomic units underlying intergroup differences, we screened differential microbiota at the phylum, genus, and species levels to determine the dysbiotic signature taxa under pathological conditions and the core responsive taxa to butyrate intervention. We further explored the associations between core differential genera and multidimensional pathological indicators via Spearman correlation analysis.

The microbiota structure was significantly dysregulated under pathological conditions. At the phylum level, the abundance of Campylobacterota was significantly increased in the IgAV model group compared with the CON group (Figure 10A). At the genus level, genera such as *norank_f__Prevotellaceae*, *Muribaculum* and *Petroclostridium* were significantly enriched, while the abundance of *Phocaeicola* was significantly decreased (Figure 10C). Changes at the species level were consistent with those at the genus level (Figure 10G). Butyrate intervention reversed the microbial dysbiosis in the model group in a treatment-specific manner, with *C. butyricum* intervention showing the most prominent ameliorative effect: at the phylum level, the abundance of Verrucomicrobiota was significantly lower than that in the model group (Figure 10B); at the genus level, it enriched the butyrate-producing genus *Allobaculum* and downregulated model-enriched genera such as *Muribaculum*, *Prevotellamassilia* and *Bacteroides* (Figure 10D); at the species level, this corresponded to increased abundances of *Allobaculum mucilyticum* and *Muricoprocola aceti*, and decreased abundances of *Akkermansia muciniphila* and *Prevotellamassilia muciniphila* (Figure 10H). Medium-dose NaB (500 mg/kg) upregulated Clostridial taxa such as *Pseudoclostridium* and Candidatus_Soleaferrea, but further reduced the abundance of

457 *Ligilactobacillus* and *Ligilactobacillus murinus* (Figure 10E, I). High-dose NaB (1000
458 mg/kg) mainly upregulated *norank_o__Eubacteriales* at the genus level (Figure 10F).
459 In normal rats under physiological conditions, butyrate exerted only a mild regulatory
460 effect on the microbiota and did not induce global structural dysregulation. *C.*
461 *butyricum* intervention significantly upregulated the abundance of *Ligilactobacillus* at
462 the genus level, and differences were observed in low-abundance taxonomic units such
463 as Actinomycetota and Pseudomonadota at the phylum level (Figure S2A, C). The
464 modulation of normal microbiota by NaB was dose-dependent: both medium and high
465 doses significantly increased the abundance of *Ligilactobacillus*, while the high dose
466 was accompanied by decreased abundance of *Verrucomicrobiota*. Overall, the
467 regulation was characterized by the upregulation of commensal beneficial bacteria
468 (Figure S2B, E–H).

469 Spearman correlation heatmaps further revealed the associations between
470 differential microbiota and pathological indicators. For intestinal barrier function, the
471 abundances of *norank_f__Prevotellaceae* and *unclassified_f__Oscillospiraceae* were
472 significantly negatively correlated with the level of tight junction protein ZO-1, and
473 significantly positively correlated with Ki-67 proliferation level and plasma LPS
474 concentration; *unclassified_f__Oscillospiraceae* was significantly negatively
475 correlated with mucin MUC2 level, while *Fuscatenibacter* abundance was significantly
476 positively correlated with MUC2 level (Figure 10J). For renal inflammatory indicators,
477 the relative abundance of *norank_f__Prevotellaceae* was significantly positively
478 correlated with IL-6, IL-21, and *Il17a* mRNA; *unclassified_f__Oscillospiraceae* was
479 also significantly positively correlated with *Il17a* mRNA, and *Ruminococcus* was
480 significantly positively correlated with IL-6 (Figure 10K). For humoral immune
481 response, the abundances of *norank_f__Prevotellaceae* and

unclassified_f__Oscillospiraceae showed a positive correlation trend with the proportion of Tfh17 cells, the proportion of IgA^+ B cells and the level of effector cytokine IL-21, among which the correlations of some indicators reached statistical significance (Figure 10L). For renal function injury, the abundances of these two genera were significantly positively correlated with URBC, UPCR, SCr and renal IgA deposition level (Figure 10M).

In summary, dysregulated genera enriched in the model group, such as *norank_f__Prevotellaceae* and *unclassified_f__Oscillospiraceae*, showed consistent positive correlations with multidimensional pathological indicators. This suggests a synergistic trend between gut microbiota composition changes and IgAV pathological alterations, indicating that microbial dysbiosis and renal injury may be linked via the gut-kidney axis.

3. Discussion

The regulatory role of gut microbiota-derived metabolites in host immune homeostasis is continually expanding the boundaries of etiological research on autoimmune diseases[1,27]. Multiple clinical studies in recent years have observed characteristic structural alterations in the gut microbiota of children with IgAV; however, systematic evidence for a causal link between microbiota dysbiosis and the disease remains scarce[28–30]. This study integrates clinical multi-omics correlation data with interventional validation in an OVA-induced rat model, confirming that reduced functional potential of butyrate-producing bacteria and insufficient butyrate levels serve as key upstream drivers of IgAV pathogenesis. This finding aligns closely with reports of specific depletion of butyrate-producing bacteria in autoimmune diseases such as systemic lupus erythematosus (SLE) and rheumatoid arthritis[31,32]. Notably,

prevailing evidence suggests that the immunoprotective effects of butyrate are primarily mediated by modulating the Th17/Treg cell balance[33,34]; however, our results indicate that the regulation of Tfh17 cell differentiation and the IgA humoral immune response by butyrate represents a critical mechanism underlying its protective effects in IgAV, and this effect is at least partially mediated by the GPR43 receptor. This divergence in effector targets suggests that the immunomodulatory effects of butyrate are markedly disease context-dependent. While these findings define the specific signaling pathway through which butyrate exerts its effects in IgAV, the structural and functional defects of the gut microbiota underlying diminished butyrate levels remain to be systematically characterized.

To address this gap in upstream mechanistic understanding, we performed a multidimensional analysis integrating metagenomic sequencing with targeted metabolomics. Our results demonstrate that gut microbiota dysbiosis in children with IgAV is not a random global structural perturbation, but a selective functional defect centered on the butyrate metabolic pathway. At the taxonomic level, core butyrate-producing genera including *Roseburia* and *Butyricicoccus* were significantly depleted; at the functional level, KEGG butyrate biosynthetic pathways and their key terminal enzymes showed a concurrent downward trend; at the metabolomic level, among the seven detected SCFAs, only butyrate exhibited a specific and significant reduction, whereas no consistent alterations were observed for the remaining metabolites. Findings across these three dimensions are mutually corroborative. A plausible explanation is that most butyrate-producing bacteria belong to strictly anaerobic Clostridia, which exhibit poor tolerance to inflammation-driven elevations in luminal oxygen tension, oxidative stress, and disrupted pH homeostasis[35,36]. Clinical association analysis revealed that fecal butyrate levels were negatively correlated with markers of

disease activity and renal injury, including 24-hour urinary protein, plasma IgA, and IL-6. This suggests that reduced butyrate levels are not merely a metabolic marker of gut microbiota dysbiosis, but may directly contribute to inflammatory amplification and tissue damage in IgAV. This aligns with the well-documented bidirectional crosstalk between inflammation and the gut microbiota[37], whereby persistent intestinal mucosal inflammation selectively reshapes microbial structure[38] and drives a progressive decline in butyrate-producing capacity[39]. We propose a vicious cycle hypothesis wherein the depletion of butyrate-producing bacteria leads to insufficient butyrate production, which in turn exacerbates intestinal inflammation and further impairs microbial functional capacity. This hypothesis accounts for the chronic relapsing nature and infection-triggered exacerbation of IgAV from a microbial ecology perspective. However, given the cross-sectional design of this study, this causal hypothesis requires further validation in prospective cohort studies.

Building on clinical association evidence, this study established an OVA-induced IgAV rat model and performed validation using two complementary strategies: exogenous NaB intervention and endogenous colonization with *C. butyricum*. The results showed that both interventions separately alleviated multi-organ immunopathological damage in rats. The protective effect of NaB presented a clear dose-dependent pattern, with the high dose exhibiting superior efficacy to the low dose, suggesting that the protective action is directly related to butyrate levels. Regarding their modes of action, exogenous NaB directly provides the active metabolite and exerts rapid effects; *C. butyricum* functions by reshaping gut microbiota structure and enhancing endogenous butyrate synthesis[40], representing a microecological regulatory pattern closer to physiological conditions. Rat fecal 16S rRNA sequencing results corroborated these findings: both interventions restored the abundance of core butyrate-

producing bacteria in the intestines of model rats, while concurrently downregulating the levels of proinflammatory bacterial genera. From the perspective of intervention response, this further supports the inference that microbiota dysbiosis participates in IgAV disease progression. Notably, the dysbiotic signature of model rats, characterized by impaired butyrate-producing function and enrichment of proinflammatory bacteria, was highly consistent with the functional alterations of gut microbiota in children with IgAV. This suggests that defective butyrate-producing function is a pathological feature conserved across species in IgAV, further reinforcing the central role of gut microbiota dysbiosis in disease pathogenesis.

After demonstrating the disease-protective effects of butyrate, we further dissected its underlying mechanisms at the gut–immune axis interface, where the intestinal barrier serves as the first line of defense[41]. We observed that colonic expression of the tight junction protein ZO-1 and the mucin MUC2 was significantly downregulated in the IgAV rat model, indicating overt structural impairment of the intestinal barrier. This is consistent with previous studies documenting intestinal barrier structural damage in IgAV and IgA nephropathy[42–44]. Notably, the co-occurrence of elevated Ki-67-positive epithelial cells and unabated barrier dysfunction in this model presents a seemingly paradoxical phenotype. This reflects compensatory epithelial proliferation triggered by ongoing mucosal damage; yet under sustained inflammatory stress, accelerated epithelial turnover alone fails to restore functional barrier integrity, consistent with the canonical paradigm of partially uncoupled signaling between proliferation and tight junction assembly in chronic immune-mediated intestinal injury[45,46]. Importantly, butyrate-mediated barrier restoration is tightly synchronized with the alleviation of systemic immune dysregulation and multi-organ injury, a concordance indicating that

its barrier-protective effect depends critically on resolving upstream inflammatory damage rather than merely enhancing epithelial renewal. In line with this tight barrier–inflammation coupling, temporal evidence from inflammatory bowel disease demonstrates that increased barrier permeability precedes clinical relapse and acts as an upstream predictor of inflammatory progression[47,48], and we reason that intestinal barrier damage is not merely a passive secondary lesion, but may represent an active contributor to inflammatory amplification and disease progression. Prior studies have established that butyrate is the primary energy substrate for colonic epithelium, supplying approximately 70% of epithelial energy requirements[49], and can upregulate the transcription and expression of tight junction proteins via GPR43 signaling[50]. Consistently, systemic *Gpr43* knockout mice exhibit impaired intestinal barrier function under inflammatory challenge[51], further supporting the central role of GPR43 signaling in maintaining intestinal barrier homeostasis. Building on these findings, we propose a hypothetical pathological amplification cascade, whereby depletion of butyrate-producing bacteria leads to butyrate insufficiency, which in turn causes epithelial energy deficit and defective tight junction assembly, elevates intestinal permeability, and drives sustained translocation of luminal antigens and microbiota-associated molecular patterns (MAMPs) into the bloodstream, ultimately providing positive feedback to perpetuate systemic immune and inflammatory activation.

Intestinal barrier disruption drives sustained translocation of luminal antigens and MAMPs into the bloodstream, which broadly triggers systemic innate immune responses[42,52]. Specifically, excessive activation of the NF-κB and/or mediated NLRP3 inflammasome acts as a key effector mechanism that progressively amplifies signals from local intestinal microbiota dysbiosis and ultimately mediates systemic multi-organ

damage[53,54]. Previous studies have confirmed that NLRP3 activation is a core event underlying endothelial injury and renal inflammation progression in IgA vasculitis and IgA nephropathy[55,56]; however, the specific molecular mechanisms by which dysregulated microbial metabolism modulates this inflammatory pathway, as well as its bridging role in mediating distant organ damage, remain to be elucidated.

Our results indicate that butyrate exerts dual anti-inflammatory effects via the GPR43 receptor: at the intestinal epithelial level, it restores barrier integrity and reduces antigen and MAMP translocation, thereby alleviating inflammatory stimulation at its source; at the myeloid cell level, butyrate inhibits NF-κB nuclear translocation via GPR43, blocks the transcriptional activation of the NLRP3 inflammasome, and concurrently downregulates the release of downstream proinflammatory cytokines including IL-1β. This dual action bears promising therapeutic value: whereas conventional anti-inflammatory drugs mostly block only downstream inflammatory signals, butyrate simultaneously targets two critical steps—antigen leakage and inflammatory activation[57]. Such multi-target synergistic regulation has also been verified in other autoimmune diseases[58,59], which aligns with the favorable safety profile of this endogenous metabolite.

Pro-inflammatory cytokines, particularly IL-6, released by innate immune cells further act on $CD4^+$ T cells in draining lymphoid organs, driving adaptive immune dysregulation and promoting robust production of pathogenic IgA. This represents a critical link connecting upstream inflammation to downstream damage in the "multiple-hit" hypothesis[60,61]. We observed a significant elevation in the frequency of Tfh17 cells in the mesenteric lymph nodes, spleen, and peripheral blood of IgAV rats, which positively correlated with IgA levels at the corresponding sites, suggesting that aberrant

Tfh17 cell expansion is a key effector event underlying humoral immune dysregulation. In accordance with the classical theory of mucosal immunity, effector T cells enter the peripheral circulation after differentiation in draining lymph nodes[62]; we speculate that inflammatory disruption of the mesenteric lymph node microenvironment may act as an upstream trigger for the systemic expansion of Tfh17 cells[63]. Mechanistically, the IL-6/STAT3 signaling pathway drives differentiation of the Tfh17 subset, which co-expresses the transcription factors Bcl-6 and RORγt[21,64]. Our data confirm that butyrate inhibits IL-6 secretion by innate immune cells via GPR43 receptor activation, thereby downregulating the phosphorylation and activation status of the IL-6/STAT3 pathway, suppressing Tfh17 cell differentiation, and ultimately reducing pathogenic IgA production to achieve upstream regulation of humoral immune abnormalities. Previous studies have largely focused on endogenous glycosylation defects in B cells and have not fully elucidated the upstream immune triggers driving sustained excessive B-cell activation[65]. The present study is the first to establish a direct link between Tfh17 cell dysregulation and the gut microbiota–butyrate axis, providing a novel perspective for dissecting the upstream mechanisms of humoral immune dysregulation in IgAV.

Building on the progressive regulatory relationships among barrier impairment, innate immune activation, and adaptive immune dysregulation, a complete pathogenic cascade can be delineated, whereby defective butyrate-producing bacterial function leads to butyrate insufficiency, which in turn drives intestinal barrier leakage and hyperactivation of the NF-κB/NLRP3 pathway, followed by excessive IL-6 secretion, aberrant Tfh17 cell expansion, dysregulated B-cell class switching, robust production of pathogenic IgA, and ultimately immune complex deposition. This cascade precisely fills the most upstream gap in the classic "multiple-hit" pathological cascade, providing a clear initial triggering mechanism for the sustained aberrant activation of B cells.

Notably, IL-6 acts as a critical regulatory node at the interface of innate and adaptive immunity, mediating bidirectional cascade amplification of inflammatory signals. In the forward regulatory arm, NF-κB activation initiates IL-6 synthesis at the transcriptional level and promotes its secretion[66], which in turn drives the differentiation of $CD4^+$ T cells toward the Tfh17 lineage[20]. In the reverse regulatory arm, IL-17A secreted by Tfh17 cells amplifies pathogenic T-cell responses by recruiting myeloid cells[67] and concurrently induces IL-6 production to reinforce upstream forward signaling[68]. Collectively, these two interlinked regulatory arms constitute a closed positive inflammatory feedback loop. This aligns with the previously described "microbiota–inflammation" vicious cycle, and together they account for the clinical features of IgAV, including persistent progression and susceptibility to relapse. Nevertheless, this reverse positive feedback loop currently remains a working hypothesis based on shared mechanisms across diseases. Its objective existence in IgAV and its responsiveness to butyrate intervention still require further validation via loss-of-function experiments. Taken together, the proposed pathogenic cascade from butyrate insufficiency to multi-organ vasculitic damage, as well as the multi-target protective effects of butyrate via the GPR43 receptor, are schematically summarized (Figure 11).

From a clinical translational perspective, this mechanistic framework further supports the utility of fecal butyrate quantification combined with metagenomic profiling of butyrate-producing taxa as a promising noninvasive biomarker panel for assessing IgAV disease activity and predicting renal injury risk. The safety of butyrate-producing probiotics, exemplified by *C. butyricum*, which are already widely used in pediatric clinical practice, has been well established[69,70], and they hold translational potential for adjunctive therapy and relapse prevention in IgAV.

Several limitations of this study should be acknowledged. First, the specific mediating role of GPR43 across distinct cell subsets remains undefined, and the contributions of alternative pathways, including HDAC inhibition and GPR109A signaling, have not been systematically dissected; further validation via tissue-specific gene knockout, receptor antagonism, or pathway blockade experiments is warranted. Second, the cross-sectional design of the clinical cohort precludes definitive conclusions regarding temporal causality. Furthermore, the OVA-induced model differs from human spontaneous disease in terms of pathogenic triggers and clinical outcomes; accordingly, our conclusions require corroboration in prospective cohorts and larger-scale clinical studies. Third, our analysis was based on fecal microbiota, which may not fully recapitulate the functional status of mucosa-associated microbiota that directly interacts with the intestinal barrier. Fourth, metagenomic sequencing only reflects the functional potential of the microbiota; the actual *in vivo* metabolic activity of butyrate biosynthesis requires further verification via metatranscriptomic or metabolic flux analyses. Despite these limitations, this study refines the classic "multiple-hit" pathogenic cascade of IgAV from a gut microbial ecology perspective, expanding etiological understanding from a narrow focus on "intrinsic B-cell abnormalities" to a holistic framework of "gut–immune axis dysregulation". These findings provide a more robust theoretical basis and experimental foundation for gut microbiota-targeted interventions in IgAV.

4. Materials and Methods

4.1 Ethical Statement

All animal procedures were performed in strict accordance with the National Institutes of Health (NIH) *Guide for the Care and Use of Laboratory Animals* and the *Animal*

Research: Reporting of In Vivo Experiments (ARRIVE) guidelines, and the experimental protocols were reviewed and approved by the Institutional Animal Care and Use Committee of Ningxia Medical University (IACUC-2025250). The clinical study was conducted in strict accordance with the ethical principles of the Declaration of Helsinki, and the study protocol was reviewed and approved by the Ethics Committee of the General Hospital of Ningxia Medical University (KYLL-2025-0215). Written informed consent was obtained from the legal guardians of all enrolled subjects.

4.2 Clinical Study

4.2.1 Study Population and Sample Collection

Study cohort enrollment This single-center observational cohort consecutively enrolled 117 children with active IgAV from the General Hospital of Ningxia Medical University. Eligible patients met the EULAR/PRINTO/PReS 2008 Ankara classification criteria, were aged 3–14 years, and presented with active-stage disease (newly diagnosed or relapsing with active purpura or organ involvement within 1 week). Uniform exclusion criteria were applied: antibiotics, probiotics, glucocorticoids or immunosuppressants within 3 months before enrollment; concurrent allergic disease, acute infection, autoimmune disorders, or primary hepatorenal dysfunction.

Clinical stratification and laboratory testing Per pediatric IgAV diagnostic guidelines[71], patients were stratified into IgAV with nephritis (IgAVN, n = 59) and non-renal IgAV (n = 58). IgAVN was defined by at least one of the following: (i) proteinuria, defined as 24-h urinary protein >0.3 g or first-morning urinary albumin/creatinine ratio >30 mg/mmol; (ii) hematuria, defined as >5 erythrocytes per high-power field on centrifuged urinary sediment microscopy; (iii) presence of erythrocyte casts in urinary sediment. Fasting venous blood and 24-h urine samples

were collected from all patients for centralized standardized testing, with values referenced to the institutional upper limit of normal.

Fecal sample collection and multi-omics subcohort For gut microbiome profiling, we established a nested age- (±1 year) and sex-matched (1:1) case-control subcohort from the 117-patient cohort. Eligibility required valid pre-treatment fresh fecal specimens and complete baseline clinical data and routine laboratory measurements; 30 eligible IgAV patients were included, paired with 30 healthy controls recruited from routine health examinations at the same center under identical exclusion criteria. Fresh fecal samples were immediately aliquoted, snap-frozen in liquid nitrogen, and stored at −80 °C.

All 60 participants underwent metagenomic sequencing, with all raw data deposited in NCBI SRA (BioProject: PRJNA1516100). Fecal SCFA quantification and paired clinical assays were performed in parallel. The 30 subcohort patients showed comparable demographic and clinical characteristics to the overall cohort, confirming sample representativeness.

Quality control and final analytical cohort After all assays, a second round of quality control was applied to ensure data completeness and minimize bias from low-quality measurements. Exclusion criteria included insufficient sequencing depth, failed SCFA detection, or missing key study-specific assay variables. Five IgAV participants were excluded, and 5 matched controls were removed accordingly per the 1:1 pairing rule. Age and sex did not differ significantly between excluded and retained participants across both groups; disease severity was comparable within the IgAV group. The final analytical cohort of 50 participants (25 IgAV, 25 controls) remained age- and sex-matched for all downstream analyses.

4.2.2 Fecal Metagenomic Sequencing

Total genomic DNA was extracted from fecal samples. After passing quality control, sequencing libraries were constructed and subjected to paired-end 150 bp (PE150) high-throughput sequencing using the NovaSeq X Plus platform. Raw data from the sequencer were processed using Trimmomatic for quality control, MEGAHIT for assembly, and Prodigal for gene prediction. Subsequently, DIAMOND software was used to align the data against the NCBI NR, Kyoto Encyclopedia of Genes and Genomes (KEGG), and Gene Ontology (GO) databases to complete species classification and functional annotation, with a focus on analyzing inter-group differences in bacterial communities and pathways related to butyrate synthesis.

4.2.3 LC-MS/MS Analysis of SCFAs in Feces

After grinding and extraction, followed by 3-nitrophenylhydrazine derivatization, fecal samples were analyzed using an ExionLC-AE / Triple Quad™ 6500+ liquid chromatography–tandem mass spectrometry (LC-MS/MS) system (AB SCIEX, USA) with Kinetex C8 columns for separation. The concentrations of seven SCFAs, namely acetic acid, propionic acid, isobutyric acid, butyric acid, isovaleric acid, valeric acid, and caproic acid, were quantified using the standard curve method. All standards were purchased from Shanghai Yuanye Biotechnology Co., Ltd.

4.3 Animal Experiments

4.3.1 Experimental rats

A total of 64 male specific pathogen-free (SPF) Sprague-Dawley (SD) rats, aged 3–4 weeks and weighing 75–95 g, were purchased from the Experimental Animal Center of Ningxia Medical University. The rats were housed in a temperature- and humidity-

controlled barrier environment with the following conditions: temperature 22 ± 2 °C, relative humidity 50% ± 10%, and a 12-hour light/dark cycle; they had free access to food and water. The formal experiment began after a 1-week acclimatization period.

4.3.2 Strain and Reagent Preparation

Clostridium butyricum (*C. butyricum*) (China General Microbiological Culture Collection Center, CGMCC, 1.5205, China) was inoculated into modified peptone-yeast extract-glucose (PYG) medium and incubated in an anaerobic incubator at 37 °C for 24 h. The bacterial suspension was washed with sterile saline, resuspended, and adjusted to a concentration of 1×10^8 colony-forming units (CFU)/mL for later use. Sodium butyrate (NaB, Sinopharm Chemical Reagents Co., Ltd., China) was prepared as working solutions at corresponding concentrations with sterile saline immediately before use.

4.3.3 Establishment of the IgAV Rat Model

An OVA-induced IgAV rat model was established according to a previously reported classical method[72]. Rats in the model group received intraperitoneal injections of an equal-volume emulsion of OVA (Solarbio, IO8050, China) and Freund's Complete Adjuvant (CFA) (Sigma-Aldrich, F5881, USA). The emulsion was administered at an OVA dose of 10 mg/kg once weekly for 3 consecutive weeks; in the fourth week, rats in the model group received a 0.25 mL tail vein injection of a 10 mg/mL OVA saline solution, along with intradermal injections at five sites on the back totaling 1 mL of a 0.3% OVA saline solution. Rats in the control group received an equal volume of saline following the same procedure.

4.3.4 Experimental Groups and Intervention Protocol

Rats were randomly divided into 8 experimental groups (n = 8 per group) using a random number table. All interventions were administered via intragastric gavage once daily for 4 consecutive weeks, with group assignments as follows: (i) normal control (CON), equal volume of sterile saline; (ii) CON + *C. butyricum*, 1×10^8 CFU/mL *C. butyricum* suspension (10 mL/kg); (iii) CON + 500 mg/kg NaB; (iv) CON + 1000 mg/kg NaB; (v) IgAV model, equal volume of sterile saline; (vi) IgAV + *C. butyricum*, same dose as group (ii); (vii) IgAV + 500 mg/kg NaB; and (viii) IgAV + 1000 mg/kg NaB. Body weight was measured and recorded at a fixed time point weekly throughout the intervention period.

4.3.5 Sample Collection and Processing

At the end of the 4-week intervention, 24-hour urine samples were collected in metabolic cages. Urine volume was recorded, and samples were centrifuged to harvest the supernatant, which was stored at −80 °C until use. At the experimental endpoint, rats were anesthetized by isoflurane inhalation, and blood was collected via cardiac puncture. After ethylenediaminetetraacetic acid (EDTA) anticoagulation, plasma was isolated by centrifugation at 600×g for 10 min at 4 °C, aliquoted, and stored at −80 °C. Following euthanasia under anesthesia, the kidneys, dorsal skin, small intestine, and colon were rapidly dissected and rinsed with ice-cold normal saline. Portions of each tissue were fixed in 4% paraformaldehyde for 24 h for histopathological analysis, while the remaining tissues were snap-frozen in liquid nitrogen and stored at −80 °C for subsequent molecular biology assays.

4.3.6 Biochemical Assays for Renal Function

Commercially available test kits (Nanjing Jiancheng Bioengineering Institute, China) were used to measure renal function parameters: urinary urea nitrogen (UUN) was

determined using the urease method; serum creatinine (SCr) and urinary creatinine (UCr) were determined using the sarcosine oxidase method; urinary total protein (UTP) was determined using the Coomassie Brilliant Blue method; urinary red blood cells (URBCs) were counted via microscopic examination of urine sediment. The urinary protein-to-creatinine ratio (UPCR) was calculated based on the test results. All procedures were performed in strict accordance with the kit instructions.

4.3.7 Histological and Immunohistochemical Analysis

After routine dewaxing and rehydration of paraffin sections, they were processed separately according to the following protocols.

Routine histological staining Skin, kidney, and colon tissues were directly stained using the HE staining kit (Servicebio, G1005, China); kidney tissues were additionally stained using the PAS staining kit (Solarbio, G1281, China). Pathological morphology was observed under a light microscope.

Immunohistochemistry (IHC) and immunofluorescence (IF) staining After high-temperature and high-pressure antigen retrieval in 10 mmol/L citrate buffer (pH 6.0) and thorough washing with PBS, sections were processed separately as follows:

IHC Endogenous peroxidase was blocked with 3% H_2O_2, followed by blocking with 5% goat serum at room temperature for 1 h. Anti-complement component 3 (C3) primary antibody (1:1000 dilution, Abcam, ab200999, UK) was applied to skin, kidney, and small intestine tissues; Ki-67 primary antibody (1:200 dilution, Immunoway, YM8189, USA) was additionally applied to colon tissues, followed by overnight incubation at 4 °C. The following day, after washing with PBS, horseradish peroxidase (HRP)-labeled goat anti-rabbit secondary antibody (1:200 dilution, Servicebio,

GB23303, China) was added and incubated at 37 °C for 1 h; diaminobenzidine (DAB) was used for color development, followed by hematoxylin counterstaining, dehydration, clearing, and slide mounting. Images were captured under a light microscope.

IF Sections were blocked with 5% BSA at room temperature for 1 h. Anti-IgA primary antibody (1:100 dilution, Abcam, ab97184, UK) was applied to skin, kidney, and small intestine tissues. Colon sections were single-stained for ZO-1 (1:200 dilution, Proteintech, 21773-1-AP, China) and MUC2 (1:1000 dilution, Proteintech, 27675-1-AP, China) respectively, and incubated overnight at 4 °C in the dark. The following day, corresponding fluorescent secondary antibodies were added and incubated at 37 °C in the dark for 1.5 h; after washing with PBS, nuclei were stained with DAPI for 5 min, and slides were mounted with anti-fade mounting medium. Images were captured using an Olympus APX-100 fluorescence microscope (Olympus, Japan).

4.3.8 Inflammatory Mediators and Immunoglobulin Assays

Plasma lipopolysaccharide (LPS) assay Plasma LPS concentrations were determined using a test-tube quantitative chromogenic substrate limulus amebocyte lysate (LAL) kit (Xiamen Limulus Reagent Biotech Co., Ltd., China). Absorbance was measured at 545 nm with a Thermo Scientific microplate reader, and concentrations were calculated via the standard curve method.

Enzyme-linked immunosorbent assay (ELISA) ELISA was performed to detect the levels of inflammatory cytokines in plasma and renal tissue homogenates, as well as plasma IgA levels. Kits for interleukin-6 (IL-6), interleukin-18 (IL-18), tumor necrosis factor-α (TNF-α) and IgA were purchased from Elabscience Biotechnology Co., Ltd. (Wuhan, China); kits for interleukin-10 (IL-10), interleukin-1β (IL-1β) and

867 interleukin-21 (IL-21) were purchased from Jianglai Biotechnology Co., Ltd.
868 (Shanghai, China). The absorbance was measured at 450 nm using a microplate reader,
869 and sample concentrations were calculated according to the standard curve.

870 **4.3.9 Real-Time Quantitative Polymerase Chain Reaction**

871 Total RNA was extracted from renal tissues using a total RNA extraction kit (Omega,
872 R6834-01, USA), and cDNA was synthesized using a reverse transcription kit
873 (TaKaRa, RR092A, Japan). With *Actb* (β-actin) as the internal reference gene, real-time
874 quantitative PCR (RT-qPCR) amplification was performed using the TB Green method.
875 The relative expression level of each target gene was calculated using the $2^{-\Delta\Delta Ct}$
876 method. The target genes included *Il6*, *Tnf*, *Il1b*, *Il18*, *Ffar2* (encoding GPR43), *Rela*
877 (encoding the p65 subunit of NF-κB), *Nlrp3*, *Rorc* (encoding RORγt), *Il21*, *Il17a*,
878 *Cxcr5*, *Bcl6* and *Stat3*, with *Actb* serving as the internal reference gene. All primers
879 were synthesized by Sangon Biotech (Shanghai) Co., Ltd. Primer sequences are shown
880 in Table 1.

881 **Table 1.** Primer sequences for RT-qPCR

Gene	Forward Primer (5′→3′)	Reverse Primer (5′→3′)
Il6	CTTCCAGCCAGTTGCCTTCTTG	TGTTGTGGGTGGTATCCTCTGTG
Tnf	AGATGTGGAACTGGCAGAGGAG	TCAGTAGACAGAAGAGCGTGGTG
Il1b	CTCACAGCAGCATCTCGACAAGAG	TCCACGGGCAAGACATAGGTAGC
Il18	GACCGAACAGCCAACGAATCC	GTAGACATCCTTCCATCCTTCACAG
Ffar2	GGCGGGCATCAGCATAGAACG	GCCACCAGAGCAGCGATCAC
Rela	ACGATGGGACGACACCTCTACAC	GGGTCTGCTCCTGCTGCTTTG
Nlrp3	TGCAGCCTCACCTCACACTCC	CAGATCGCCCAGGTCGTTGTTG
Rorc	GAAGACCCACACCTCACAAATCG	TGGCTGCGGCGGAAGAAG
Il21	TCAGAAAGCCCAAACTCAAGCCATC	GTGCCTCTGTTTATTCCTGTCCTC

Il17a	CCTGATGCTGTTGCTGCTACTG	GCGTTTGGACACACTGAACTTTG
Cxcr5	GGTGACAAGCATCTTCCTTCTCTG	GGTAGCCACTCAATTCGCAACTG
Bcl6	AGGTCGTGAGGTTGTGGAGAAC	ATCGGATAAGAGGCTGGTGGTG
Stat3	TCCTGCTGCGGGTTCAGTGAG	GCTGCTGCTTGGTATATGGTTCTAC
Actb	TGTCACCAACTGGGACGATA	GGGGTGTTGAAGGTCTCAAA

4.3.10 Western Blotting

Total protein was extracted from renal tissues using a total protein extraction kit (KeyGEN BioTECH, KGB5303, China), and protein concentration was determined using a bicinchoninic acid (BCA) protein quantification kit (KeyGEN BioTECH, KGB2101, China). A total of 30 μg of total protein was separated by sodium dodecyl sulfate–polyacrylamide gel electrophoresis (SDS-PAGE) and electrotransferred onto a polyvinylidene fluoride (PVDF) membrane (Millipore, IPVH00010, USA). The membrane was blocked with 5% skim milk at room temperature for 2 h, then incubated with the corresponding primary antibodies overnight at 4 °C on a shaker. The primary antibodies and dilution ratios used were as follows: FFAR2 (1:1000, Proteintech, 84544-1-RR, China), Phospho-NF-κB p65 (1:1000, Proteintech, 82335-1-RR, China), NLRP3 (1:4000, Proteintech, 30109-1-AP, China), Total/Cleaved Caspase-1 (1:1000, Abmart, M025280, China), ASC (1:5000, Proteintech, 10500-1-AP, China), IL-6 (1:5000, ABclonal, A27935, China), Phospho-STAT3 (Tyr705) (1:2000, CST, 9145T, USA), Total STAT3 (1:1000, CST, 12640T, USA). After washing the membrane three times with Tris-buffered saline with Tween 20 (TBST), HRP-labeled secondary antibody was added and incubated at room temperature for 1 h. Bands were visualized using an enhanced chemiluminescence (ECL) kit (KeyGEN BioTECH, KGC4602, China), and the grayscale values of the bands were quantified using ImageJ software.

4.3.11 Flow Cytometric Analysis of Immune Cell Subpopulations

902 Single-cell suspensions were prepared from rat spleens, peripheral blood, and
903 mesenteric lymph nodes respectively, and adjusted to a concentration of 1×10^6
904 cells/mL.

905 **Detection of Tfh17 cells** CD45-APC-Cy7 (BD Pharmingen, 561586, USA), CD4-
906 FITC (Thermo, 11-0040-82, USA), CXCR5-AF647 (Santa Cruz, sc-373775 AF647,
907 USA), and CCR6-PE (R&D Systems, FAB8320P, USA) were added to the cell
908 suspension; samples were incubated at 4 °C in the dark for 30 min. Cells were
909 stimulated with cell stimulation cocktail (Thermo Fisher, 00-4970-03, USA) at 37 °C
910 for 4–6 h, then subjected to fixation and permeabilization using a fixation and
911 permeabilization kit. IL-17A-eFluor 450 antibody (eBioscience, 48-7177-82, USA)
912 was added and incubated in the dark for 30 min; cells were washed with PBS and
913 resuspended.

914 **Detection of IgA-positive B cells** CD45-APC-Cy7 (BD Pharmingen, 561586,
915 USA), CD45R-RB705 (BD OptiBuild, 757058, USA), CD3-APC (BD Pharmingen,
916 557030, USA), and IgA-FITC (AbD Serotec, MCA191F, UK) were added to the cell
917 suspension; samples were incubated at 4 °C in the dark for 30 min, washed with PBS,
918 and resuspended.

919 All samples were acquired on a CytoFLEX flow cytometer (Beckman Coulter,
920 USA), and data were analyzed using FlowJo software.

921 **4.3.12 Fecal 16S rRNA Gene Sequencing**

922 Total microbial DNA was extracted from the feces of SD rats; five rats per group were
923 randomly selected for sequencing. The full-length bacterial 16S rRNA gene was
924 amplified, and high-throughput sequencing was performed using the PacBio platform.

QIIME2 software was used to perform sequence quality control, amplicon sequence variant (ASV) clustering, and species annotation, and to analyze alpha diversity, beta diversity, intergroup differences in species abundance, as well as the correlations between the microbiota and pathological phenotypic indicators.

4.4 Statistical Analysis

Statistical analyses were performed using Prism 10.1.2 (GraphPad Software Inc., USA). All quantitative data were first subjected to the Shapiro-Wilk normality test and Levene's test for homogeneity of variances: data that were normally distributed and had homogeneous variances were expressed as mean ± standard error of the mean (SEM); comparisons among multiple groups were performed using one-way analysis of variance (ANOVA), and pairwise comparisons between groups were conducted using Tukey's post hoc test; data that did not follow a normal distribution were expressed as the median (interquartile range); comparisons among multiple groups were performed using the Kruskal-Wallis H test, and comparisons between two independent samples (including subgroup analysis of IgAV patients with and without IgAVN) were performed using the Mann-Whitney U test. Comparisons between routine clinical parameters in children with IgAV and the upper limits of normal laboratory reference ranges were performed using the one-sample Wilcoxon signed-rank test. Correlations between variables were analyzed using Spearman's rank correlation. All tests were two-sided; $P < 0.05$ was considered statistically significant.

Declarations

Ethics approval and consent to participate

This clinical study was conducted in accordance with the Declaration of Helsinki. Ethical approval was granted by the Medical Ethics Committee of the General Hospital of Ningxia Medical University (Approval No. KYLL-2025-0215). Written informed consent was obtained from the legal guardians of all enrolled pediatric participants. All animal experiments were conducted in compliance with protocols approved by the Institutional Animal Care and Use Committee (IACUC) of Ningxia Medical University, China (Approval No. IACUC-2025250), and with the NIH Guide for the Care and Use of Laboratory Animals.

Consent for publication

Not applicable.

Availability of data and materials

The 16S rRNA gene sequencing raw data have been deposited in the National Center for Biotechnology Information (NCBI) Sequence Read Archive (SRA) under accession number [PRJNA1515816]. The metagenomic sequencing raw data have been deposited in the National Center for Biotechnology Information (NCBI) Sequence Read Archive (SRA) under accession number [PRJNA1516100]. Other data supporting the findings of this study are available from the corresponding author upon reasonable request.

Competing interests

The authors declare that they have no competing interests.

Funding

This work was funded by the Ningxia Natural Science Foundation, China (Grant No. 2025AAC030870), the Ningxia Gut Homeostasis and Chronic Disease Prevention and Treatment Scientific and Technological Innovation Team, China (Grant No. 2022BSB03112), and the Program of Ningxia Science and Technology Leading Talent, China (Grant No. 2023GKLRLX17).

References

1. Rao, X., Zou, L., Cai, X., Yao, Y. & Zhong, L. Microbiome-orchestrated cross-organ immunity in autoimmunity: from metabolites to therapeutic targets. *Front Immunol* **17**, 1761834 (2026).
2. Zheng, D., Liwinski, T. & Elinav, E. Interaction between microbiota and immunity in health and disease. *Cell Res* **30**, 492–506 (2020).
3. Christovich, A. & Luo, X. M. Gut Microbiota, Leaky Gut, and Autoimmune Diseases. *Front Immunol* **13**, 946248 (2022).
4. Grice, E. A. & Segre, J. A. The human microbiome: our second genome. *Annu Rev Genomics Hum Genet* **13**, 151–170 (2012).
5. Mann, E. R., Lam, Y. K. & Uhlig, H. H. Short-chain fatty acids: linking diet, the microbiome and immunity. *Nat Rev Immunol* **24**, 577–595 (2024).
6. Wang, X. *et al.* Emerging role of gut microbiota in autoimmune diseases. *Front Immunol* **15**, 1365554 (2024).
7. Parada Venegas, D. *et al.* Short Chain Fatty Acids (SCFAs)-Mediated Gut Epithelial and Immune Regulation and Its Relevance for Inflammatory Bowel Diseases. *Front Immunol* **10**, 277 (2019).
8. Kim, C. H. Complex regulatory effects of gut microbial short-chain fatty acids on immune tolerance and autoimmunity. *Cell Mol Immunol* **20**, 341–350 (2023).
9. Wu, Q. *et al.* p38 MAP kinase senses short-chain fatty acids to attenuate Toll-like receptor signaling and intestinal inflammation. *Sci Adv* **12**, eaef1419.
10. Gage, A., Pepper, R. J., Marro, J., Salama, A. D. & Oni, L. IgA Vasculitis Across the Ages: Is It Time for a Precision Medicine Approach? *ACR Open Rheumatol* **7**, e70083 (2025).

11. Xu, L., Li, Y. & Wu, X. IgA vasculitis update: Epidemiology, pathogenesis, and biomarkers. *Front Immunol* **13**, 921864 (2022).
12. Hastings, M. C. *et al.* IgA vasculitis with nephritis: update of pathogenesis with clinical implications. *Pediatr Nephrol* **37**, 719–733 (2022).
13. Zhang, Y. *et al.* Differences in Manifestations and Gut Microbiota Composition Between Patients With Different Henoch-Schonlein Purpura Phenotypes. *Front Cell Infect Microbiol* **11**, 641997 (2021).
14. Cao, J. *et al.* Metagenomic profiling reveals dominance of gram-positive bacteria in the gut microbiome shifts associated with immunoglobulin A vasculitis (Henoch–Schönlein Purpura). *Clin Transl Immunology* **10**, e1342 (2021).
15. Held, M. *et al.* Insight into the Interplay of Gd-IgA1, HMGB1, RAGE and PCDH1 in IgA Vasculitis (IgAV). *Int J Mol Sci* **25**, 4383 (2024).
16. Huang, J., Liu, J., Hu, Y., Zhang, X. & Zhang, Q. Tfh Cells in Henoch-Schönlein Purpura (IgA Vasculitis): Current Concept. *J Immunol Res* **2026**, e4143288 (2026).
17. Qiu, H., Wu, H., Chan, V., Lau, C.-S. & Lu, Q. Transcriptional and epigenetic regulation of follicular T-helper cells and their role in autoimmunity. *Autoimmunity* **50**, 71–81 (2017).
18. Carreto-Binaghi, L. E., Sztein, M. B. & Booth, J. S. Role of cellular effectors in the induction and maintenance of IgA responses leading to protective immunity against enteric bacterial pathogens. *Front Immunol* **15**, 1446072 (2024).
19. Shen, C. & Fu, Q. Follicular helper T cells (Tfh): heterogeneity in spatial distribution and phenotypic characteristics. *Front Immunol* **16**, 1686687 (2025).
20. Jiang, Q. *et al.* Amelioration of immunoglobulin A vasculitis by suppression of the pathological expansion of T follicular helper 17 cells. *J Autoimmun* **149**, 103304 (2024).
21. Ma, X. & Nakayamada, S. Multi-Source Pathways of T Follicular Helper Cell Differentiation. *Front Immunol* **12**, 621105 (2021).
22. Crotty, S. T follicular helper cell biology: A decade of discovery and diseases. *Immunity* **50**, 1132–1148 (2019).

23. Xu, Z. *et al.* Short-chain fatty acids: key antiviral mediators of gut microbiota. *Front Immunol* **16**, 1614879 (2025).
24. Qin, H. *et al.* Gut microbiota-metabolome crosstalk in allergic diseases: mechanistic insights and translational opportunities. *Front Allergy* **6**, 1631479 (2025).
25. Zhao, Y. *et al.* GPR43 mediates microbiota metabolite SCFA regulation of antimicrobial peptide expression in intestinal epithelial cells via activation of mTOR and STAT3. *Mucosal Immunol* **11**, 752–762 (2018).
26. Takeuchi, T., Nakanishi, Y. & Ohno, H. Microbial Metabolites and Gut Immunology. *Annu Rev Immunol* **42**, 153–178 (2024).
27. Ruff, W. E., Greiling, T. M. & Kriegel, M. A. Host-microbiota interactions in immune-mediated diseases. *Nat Rev Microbiol* **18**, 521–538 (2020).
28. Liang, Y. *et al.* Taxonomic and functional shifts of gut microbiome in immunoglobulin A vasculitis children and their mothers. *Front Pediatr* **12**, 1356529 (2024).
29. Hu, X. *et al.* Landscape of intestinal microbiota in patients with IgA nephropathy, IgA vasculitis and Kawasaki disease. *Front Cell Infect Microbiol* **12**, 1061629 (2022).
30. Chen, Y. *et al.* Differential gut microbiota and inflammatory cytokines contribute to IgA vasculitis. *Clin Exp Rheumatol* **43**, 563–574 (2025).
31. Zhao, N. *et al.* Multiomics-guided discovery of protective microbiome signatures in lupus-prone mice treated with Faecalibacterium prausnitzii. *Nat Commun* **17**, 5120 (2026).
32. Zhan, J.-Y. *et al.* Recent advances in the positive role of Clostridium in autoimmune diseases: as a crucial regulator of restoring immune-metabolic equilibrium. *Front Immunol* **17**, 1730351 (2026).
33. Li, G. *et al.* Gut microbiota-derived metabolites modulate Treg/Th17 balance: novel therapeutic targets in autoimmune diseases. *Front Immunol* **16**, 1710733 (2025).
34. Li, T. *et al.* Clostridium butyricum inhibits the inflammation in children with primary nephrotic syndrome by regulating Th17/Tregs balance via gut-kidney axis. *BMC Microbiol* **24**, 97 (2024).

35. Zhang, F., Zhang, W., Ren, X., Liu, B. & Zhou, X. Butyrate-Producing Bacteria in Intestinal Disease Therapy: Potential and Challenges. *Biotechnol J* **21**, e70260 (2026).

36. Allaire, J. M. *et al.* The Intestinal Epithelium: Central Coordinator of Mucosal Immunity. *Trends Immunol* **39**, 677–696 (2018).

37. Sartor, R. B. & Wu, G. D. Roles for Intestinal Bacteria, Viruses, and Fungi in Pathogenesis of Inflammatory Bowel Diseases and Therapeutic Approaches. *Gastroenterology* **152**, 327-339.e4 (2017).

38. Byndloss, M. X. *et al.* Microbiota-activated PPAR-γ signaling inhibits dysbiotic Enterobacteriaceae expansion. *Science* **357**, 570–575 (2017).

39. Litvak, Y., Byndloss, M. X. & Bäumler, A. J. Colonocyte metabolism shapes the gut microbiota. *Science* **362**, eaat9076 (2018).

40. Liu, X. *et al.* Alteration of gut microbiome and metabolome by Clostridium butyricum can repair the intestinal dysbiosis caused by antibiotics in mice. *iScience* **26**, 106190 (2023).

41. An, J. *et al.* The Role of Intestinal Mucosal Barrier in Autoimmune Disease: A Potential Target. *Front Immunol* **13**, 871713 (2022).

42. Sun, S. *et al.* Gut microbiota in Henoch-Schönlein purpura: from pathogenesis to therapeutic strategies. *Front Immunol* **17**, 1838103 (2026).

43. Monteiro, R. C. & Berthelot, L. Role of gut-kidney axis in renal diseases and IgA nephropathy. *Curr Opin Gastroenterol* **37**, 565–571 (2021).

44. Zhao, W. *et al.* Therapeutic effect of rutin on Henoch-Schönlein purpura by attenuating inflammation and protection of the intestinal barrier function in rats. *Eur J Pharmacol* **1025**, 178946 (2026).

45. Koch, S. & Nusrat, A. The life and death of epithelia during inflammation: lessons learned from the gut. *Annu Rev Pathol* **7**, 35–60 (2012).

46. Sanchez Alvarez, R. *et al.* Intestinal epithelial PTPN23 is essential for gut barrier integrity and prevention of fatal bacterial translocation. *J Crohns Colitis* **19**, jjaf016 (2025).

47. Wyatt, J., Vogelsang, H., Hübl, W., Waldhöer, T. & Lochs, H. Intestinal permeability and the prediction of relapse in Crohn's disease. *Lancet* **341**, 1437–1439 (1993).

48. Turpin, W. *et al.* Increased Intestinal Permeability Is Associated With Later Development of Crohn's Disease. *Gastroenterology* **159**, 2092-2100.e5 (2020).
49. Sun, J. *et al.* Butyrate as a promising therapeutic target in cancer: From pathogenesis to clinic (Review). *Int J Oncol* **64**, 44 (2024).
50. Cheng, D. *et al.* Butyrate ameliorated-NLRC3 protects the intestinal barrier in a GPR43-dependent manner. *Exp Cell Res* **368**, 101–110 (2018).
51. Tang, M. *et al.* GPR43 deficiency aggravates sepsis by promoting gut microbiota-dependent barrier disruption and HIF-1α-ENO1 axis-mediated M1 polarization of macrophages. *Cell Mol Biol Lett* **31**, 12 (2025).
52. Mf, N., D, A. & C, B. The intestinal barrier: a pivotal role in health, inflammation, and cancer. *The lancet. Gastroenterology & hepatology* **10**, (2025).
53. Tan, J. *et al.* Probiotics ameliorate IgA nephropathy by improving gut dysbiosis and blunting NLRP3 signaling. *J Transl Med* **20**, 382 (2022).
54. Chen, X. *et al.* NEK7 interacts with NLRP3 to modulate the pyroptosis in inflammatory bowel disease via NF-κB signaling. *Cell Death Dis* **10**, 906 (2019).
55. Liu, Y. *et al.* TLR4 Inhibitor TAK-242 Protected Henoch-Schonlein Purpura Nephritis in Rats by Regulating Inflammatory Response and Immune Competence via NF-κB/NLRP3 Signalling. *Clin Exp Pharmacol Physiol* **52**, e70008 (2025).
56. Luo, Y., Long, M., Wu, X. & Zeng, L. Targeting the NLRP3 inflammasome in kidney disease: molecular mechanisms, pathogenic roles, and emerging small-molecule therapeutics. *Front Immunol* **16**, 1703560 (2025).
57. Liu, Z., Jiang, Y., Fan, Q., Li, S. & Wang, Y. The Role of Butyric Acid and Microorganisms in Chronic Inflammatory Diseases and Microbiome-Based Therapeutics. *J Inflamm Res* **18**, 13465–13487 (2025).
58. He, J. *et al.* Intestinal butyrate-metabolizing species contribute to autoantibody production and bone erosion in rheumatoid arthritis. *Sci Adv* **8**, eabm1511 (2022).
59. Cao, Y. *et al.* Butyrate: a bridge between intestinal flora and rheumatoid arthritis. *Front Immunol* **15**, 1475529 (2024).

60. Xie, J. *et al.* Expansion of Circulating T Follicular Helper Cells in Children with Acute Henoch-Schönlein Purpura. *J Immunol Res* **2015**, 742535 (2015).

61. Du, W. *et al.* Increased proportion of follicular helper T cells is associated with B cell activation and disease severity in IgA nephropathy. *Front Immunol* **13**, 901465 (2022).

62. Sano, T. *et al.* Redundant cytokine requirement for intestinal microbiota-induced Th17 cell differentiation in draining lymph nodes. *Cell Rep* **36**, 109608 (2021).

63. Hirota, K. *et al.* Plasticity of Th17 cells in Peyer's patches is responsible for the induction of T cell-dependent IgA responses. *Nat Immunol* **14**, 372–379 (2013).

64. Zhang, C.-J. *et al.* Act1 is a negative regulator in T and B cells via direct inhibition of STAT3. *Nat Commun* **9**, 2745 (2018).

65. Parums, D. V. A Review of IgA Vasculitis (Henoch-Schönlein Purpura) Past, Present, and Future. *Med Sci Monit* **30**, e943912 (2024).

66. Luo, Y. & Zheng, S. G. Hall of Fame among Pro-inflammatory Cytokines: Interleukin-6 Gene and Its Transcriptional Regulation Mechanisms. *Front Immunol* **7**, 604 (2016).

67. McGinley, A. M. *et al.* Interleukin-17A Serves a Priming Role in Autoimmunity by Recruiting IL-1β-Producing Myeloid Cells that Promote Pathogenic T Cells. *Immunity* **52**, 342-356.e6 (2020).

68. Ogura, H. *et al.* Interleukin-17 promotes autoimmunity by triggering a positive-feedback loop via interleukin-6 induction. *Immunity* **29**, 628–636 (2008).

69. Kim, E.-J., Go, H.-Y. & Sung, H.-K. Efficacy of Clostridium butyricum Supplementation Combined with Phototherapy for Neonatal Hyperbilirubinemia: A Systematic Review and Meta-Analysis. *Microorganisms* **13**, 1441 (2025).

70. Guo, Q., Goldenberg, J. Z., Humphrey, C., El Dib, R. & Johnston, B. C. Probiotics for the prevention of pediatric antibiotic-associated diarrhea. *Cochrane Database Syst Rev* **4**, CD004827 (2019).

71. Ozen, S. *et al.* EULAR/PRINTO/PRES criteria for Henoch-Schönlein purpura, childhood polyarteritis nodosa, childhood Wegener granulomatosis and childhood Takayasu arteritis: Ankara 2008. Part II: Final classification criteria. *Ann Rheum Dis* **69**, 798–806 (2010).

72. Li, Y. *et al.* Hematologic and immunological characteristics of Henoch-Schönlein purpura in rat and rabbit models induced with ovalbumin based on type III hypersensitivity. *Sci Rep* **5**, 8862 (2015).

Figure legends

Figure 1. Gut microbiota composition in IgAV patients and controls by metagenomic sequencing. (A) PCoA based on Bray–Curtis distance showing beta diversity. (B) Shannon index of alpha diversity. (C) Venn diagram of shared and unique microbial genes. (D–F) Relative abundance at phylum (D), genus (E), and species (F) levels. (G) Abundance of dominant phyla and the Bacillota/Bacteroidota ratio. Relative abundance of key butyrate-producing taxa at genus (H) and species (I) levels. Data are presented as mean ± SEM. *P < 0.05, **P < 0.01.

Figure 2. Gut microbiota butyrate metabolism and clinical correlations in IgAV. (A) PCoA plot of KO abundance based on Bray–Curtis distance. (B) Relative abundance of KEGG functional pathways. (C) Differentially abundant KEGG pathways related to butyrate metabolism between the two groups. (D) Differentially abundant genes encoding two key terminal enzymes for butyrate biosynthesis (butyrate-CoA transferase and butyrate kinase) between the two groups. (E) Fecal concentrations of seven SCFAs. (F) Clinical laboratory parameters in IgAV patients; the red dashed line indicates the upper reference limit. (G) Key clinical indicators in non-renal IgAV and IgAVN patients. (H) Spearman correlation analysis of fecal butyrate levels with IL-6, plasma IgA and 24h UP. (I) Spearman correlation heatmap of differential butyrate-producing genera and butyrate metabolism-related KEGG pathways. (J) Spearman correlation heatmap of differential butyrate-producing genera with 24h UP, CRP, IL-6, and plasma IgA**.** Data are expressed as mean ± SEM. *P < 0.05, **P < 0.01, ***P < 0.001.

Figure 3. Effects of *C. butyricum* and NaB on disease and renal function in IgAV rats. (A) Schematic illustration of the experimental protocol. (B) Body weight curves of rats in each group. Gross morphology of purpuric lesions on the tail (C) and dorsal skin (D). (E–H) Renal

function parameters: SCr, UUN, URBC, UTP, UCr and UPCR. Data are expressed as mean ± SD. *P < 0.05, **P < 0.01, ***P < 0.001, ****P < 0.0001.

Figure 4. Effects of *C. butyricum* and NaB on skin and renal pathology in IgAV rats. Representative histological staining images of skin tissue (×20): HE staining (A), IgA IF staining (DAPI, blue; IgA, green) (B), C3 IHC staining (C). Representative histological staining images of renal tissue (×40): HE staining (D), PAS staining (E), IgA IF staining (F), C3 IHC staining (G). Relative IgA fluorescence intensity in the skin (H) and glomeruli (J) quantified by densitometric analysis. Relative C3-positive area fraction in the skin (I) and glomeruli (K) quantified by digital image analysis. Data are expressed as mean ± SD. *P < 0.05, **P < 0.01, ***P < 0.001, ****P < 0.0001.

Figure 5. Effects of *C. butyricum* and NaB on intestinal barrier and immune deposition in IgAV rats. (A) Representative HE staining image of colonic tissue (×20). Representative histological staining images of small intestinal tissue (×20): IgA IF staining (DAPI, blue; IgA, green) (B), C3 IHC staining (C). Relative IgA fluorescence intensity in the small intestine (D) quantified by densitometric analysis, and relative C3-positive area fraction in the small intestine (E) quantified by digital image analysis. Representative histological staining images of colonic tissue (×20): (F) ZO-1 IF staining (ZO-1, red; DAPI, blue), (G) MUC2 IF staining (MUC2, green; DAPI, blue), (H) Ki-67 IHC staining. Relative ZO-1 fluorescence intensity (I), relative MUC2 fluorescence intensity (J) quantified by densitometric analysis, and Ki-67-positive cell fraction in the colon (K) quantified by digital image analysis. (L) Plasma LPS level detected by LAL assay. Data are expressed as mean ± SD. *P < 0.05, **P < 0.01, ***P < 0.001, ****P < 0.0001.

Figure 6. Effects of *C. butyricum* and NaB on inflammation and GPR43/NF-κB/NLRP3 pathway activation in IgAV rats. Plasma concentrations of IL-6 (A), TNF-α (B), and IL-1β (C) measured by ELISA. Concentrations of IL-6 (D), TNF-α (E), and IL-1β (F) in renal tissue homogenates measured by ELISA. Relative mRNA expression of *Ffar2* (G), *Rela* (H), and

Nlrp3 (I) in renal tissues quantified by qPCR. (J) Western blot analysis of FFAR2, p-P65, NLRP3, Pro-caspase-1, ASC, and IL-6 in renal tissues, with β-actin as the loading control. Densitometric semi-quantification of Western blot bands: FFAR2/β-actin (K), p-P65/β-actin (L), NLRP3/β-actin (M), Pro-caspase-1/β-actin (N), ASC/β-actin (O), and IL-6/β-actin (P). Data are expressed as mean ± SD. **P* < 0.05, ***P* < 0.01, ****P* < 0.001, *****P* < 0.0001.

Figure 7. Effects of *C. butyricum* and NaB on renal Tfh17 pathway molecules in IgAV rats. Relative mRNA expression of Tfh17-related molecules in renal tissues quantified by qPCR: *Stat3* (A), *Rorc* (B), *Bcl6* (C), and *Cxcr5* (D). Relative mRNA expression of effector cytokines in renal tissues quantified by qPCR: *Il17a* (E) and *Il21* (F). (G) Western blot analysis of p-STAT3 and total STAT3 in renal tissues, with β-actin as the loading control. (H) Densitometric semi-quantification of the p-STAT3/total STAT3 ratio. Data are expressed as mean ± SD. **P* < 0.05, ***P* < 0.01, ****P* < 0.001, *****P* < 0.0001.

Figure 8. Effects of *C. butyricum* and NaB on Tfh17 and IgA^+ B cells in IgAV rats. Flow cytometric analysis of Tfh17 and IgA^+ B cell proportions in MLN (A, B), spleen (C, D), and peripheral blood (E, F). Representative scatter plots are shown on the left, with statistical results on the right. (G) Spearman correlation analysis of Tfh17 cell proportion with IgA^+ B cell proportion in MLN, spleen, and peripheral blood. Plasma IL-21 (H), renal homogenate IL-21 (I), and plasma total IgA (J) measured by ELISA. Data are expressed as mean ± SD. **P* < 0.05, ***P* < 0.01, ****P* < 0.001, *****P* < 0.0001.

Figure 9. Effects of *C. butyricum* and NaB on gut microbiota diversity and composition in IgAV rats. Fecal samples from eight experimental groups (n = 5 per group) were analyzed by 16S rRNA gene amplicon sequencing. (A) Rarefaction curves to evaluate sequencing depth and saturation. (B) Alpha diversity indices analyzed by the Kruskal–Wallis H test. (C) PCoA plot based on Bray–Curtis distance at the ASV level. (D) Intergroup beta diversity distances analyzed by the Wilcoxon rank-sum test. (E) Venn diagram illustrating shared and unique

ASVs across the eight groups. Stacked bar plots showing the relative abundance of gut microbiota at the phylum (F), genus (G), and species (H) levels.

Figure 10. Effects of *C. butyricum* and NaB on gut microbiota and phenotypic correlations in IgAV rats. Relative abundance of differential gut microbiota at the phylum level: CON vs. IgAV (A), IgAV vs. IgAV+*C. butyricum* (B). Relative abundance of differential gut microbiota at the genus level: CON vs. IgAV (C), IgAV vs. IgAV+*C. butyricum* (D), IgAV vs. IgAV+500 mg/kg NaB (E), and IgAV vs. IgAV+1000 mg/kg NaB (F). Relative abundance of differential gut microbiota at the species level: CON vs. IgAV (G), IgAV vs. IgAV+*C. butyricum* (H), and IgAV vs. IgAV+500 mg/kg NaB (I). Spearman correlation heatmaps of differential gut microbiota with phenotypic indicators: (J) ZO-1, MUC2, Ki-67 and plasma LPS; (K) Renal IL-6, IL-21 and *Il17a* mRNA; (L) Plasma IL-6, IL-21, Tfh17 cell frequency and IgA^+ B cell frequency; (M) URBC, UPCR, SCr and plasma IgA. Data are expressed as mean ± SD. $^*P < 0.05$, $^{**}P < 0.01$, $^{***}P < 0.001$, $^{****}P < 0.0001$.

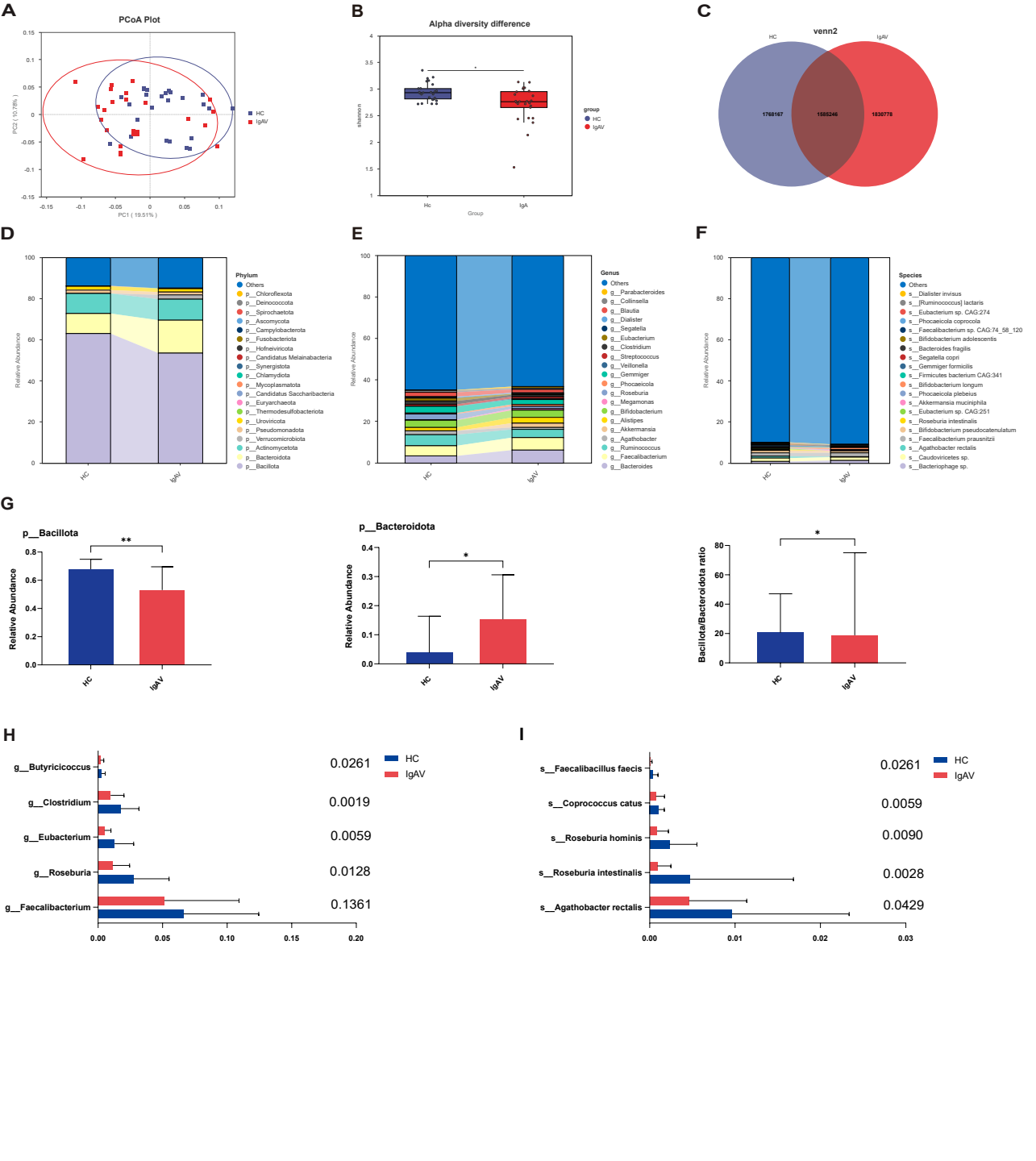
Figure 11. Protective mechanism of *C. butyricum* and NaB in IgAV via GPR43. This diagram highlights IL-6 as the core mediator bridging intestinal barrier injury and systemic immune dysregulation. Key findings: (1) *C. butyricum* and NaB restore intestinal barrier integrity, inhibit LPS-driven NF-κB/NLRP3 activation, and reduce pro-inflammatory IL-6 secretion; (2) Butyrate targets the IL-6/STAT3/Tfh17 immune axis to suppress aberrant IgA production. These effects collectively attenuate multi-organ damage in IgAV.

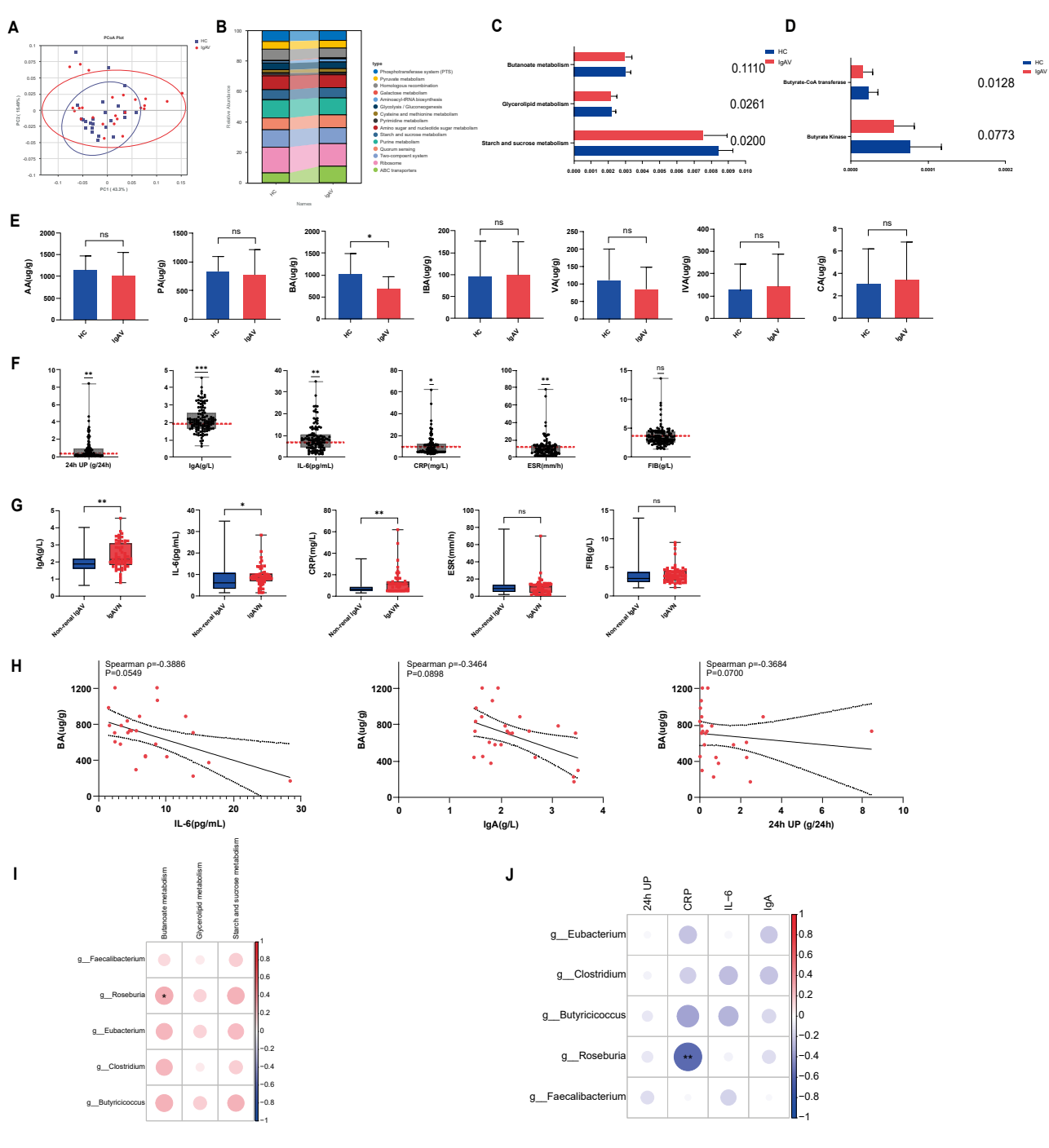
Supplementary Information

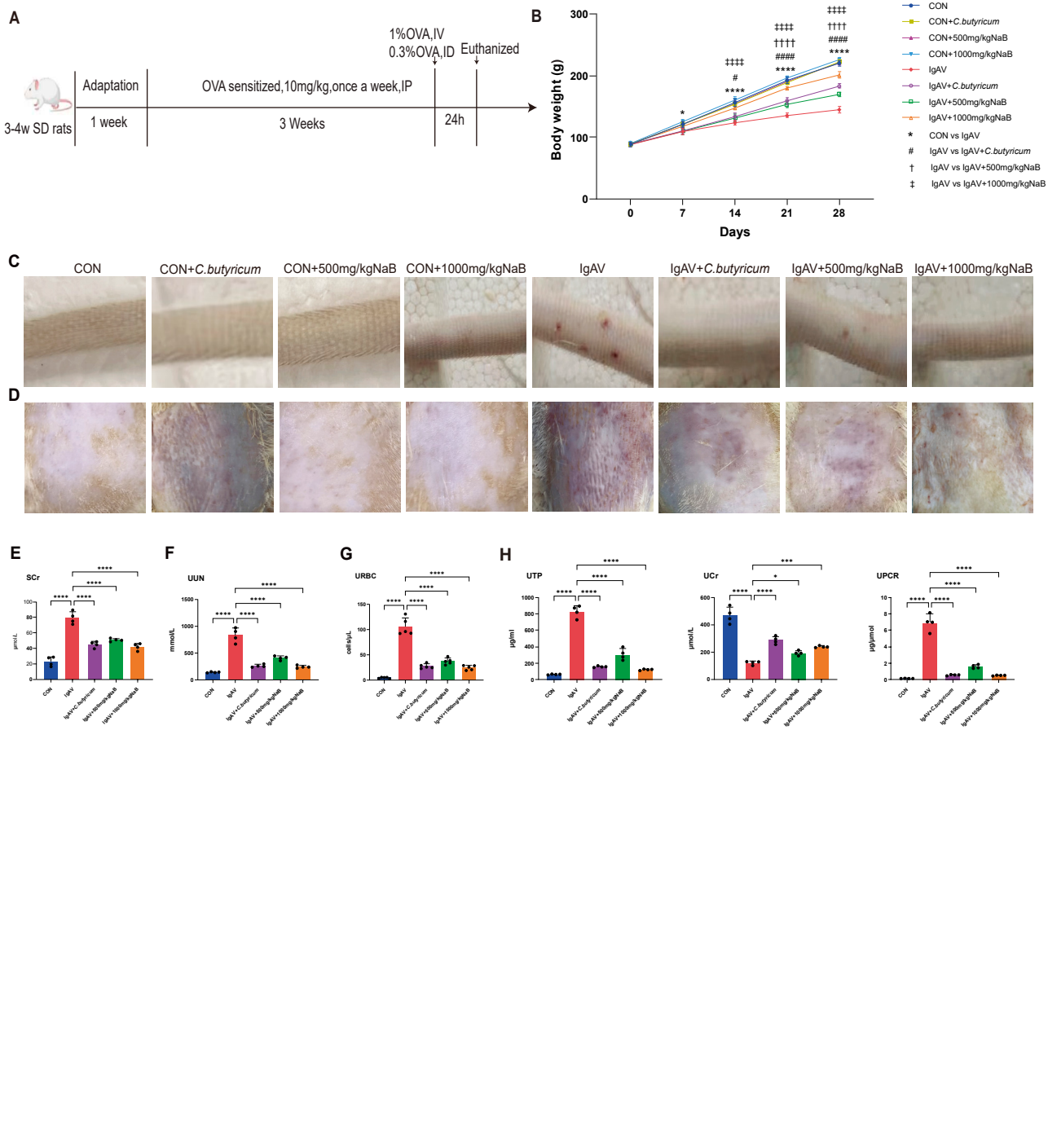
Supplementary information is available in the online version of the article.

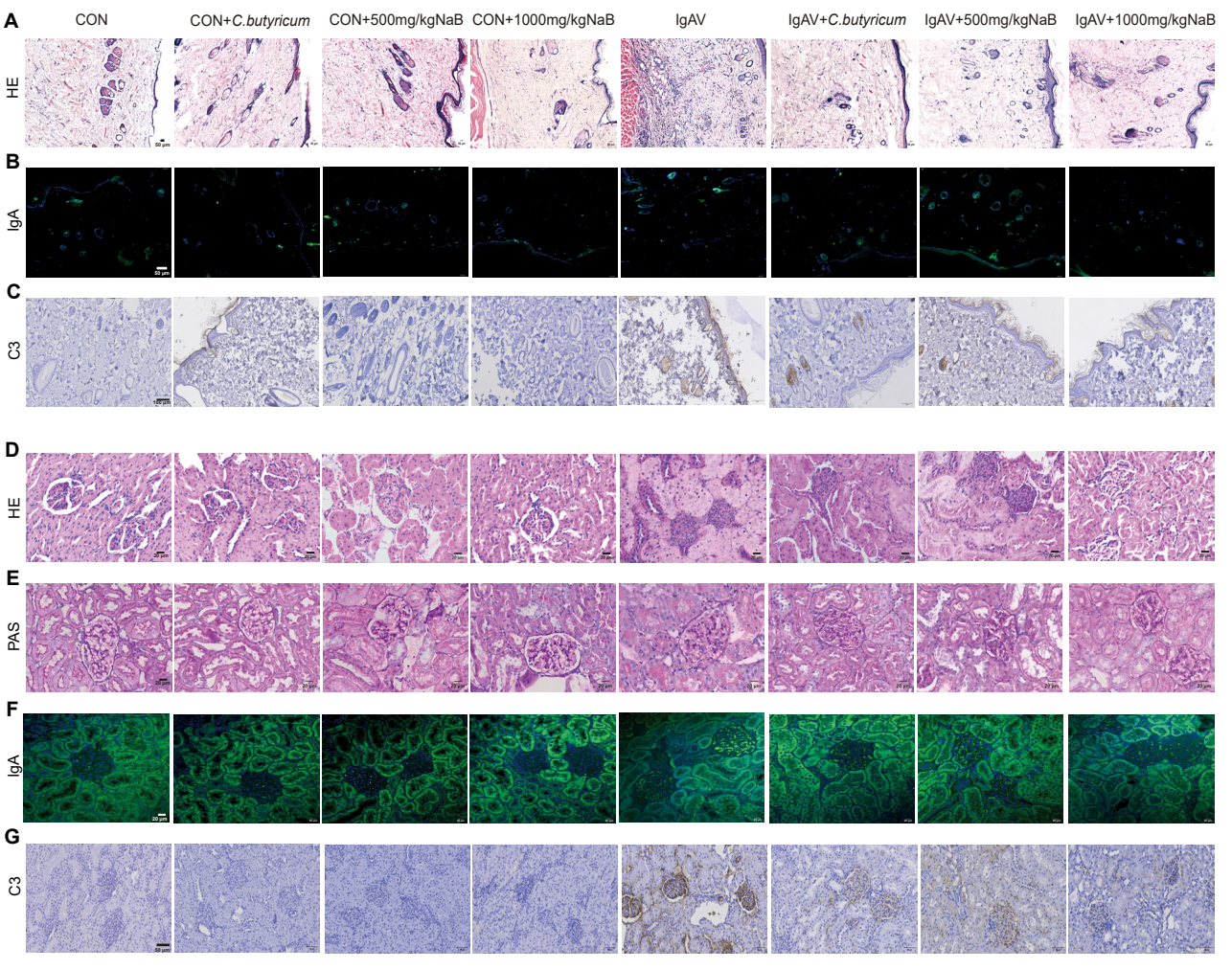
Figure S1. Effects of *C. butyricum* and NaB on plasma and renal inflammatory cytokines in IgAV rats.

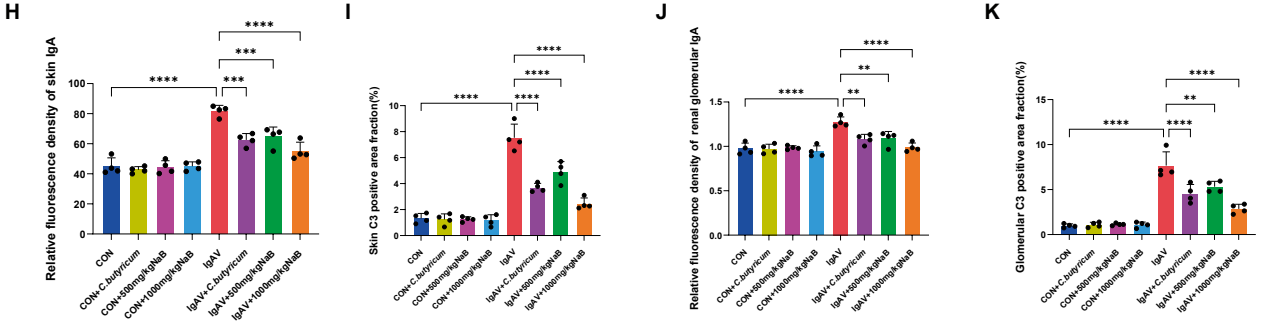
Figure S2. Effects of *C. butyricum* and NaB on gut microbiota composition in control rats.

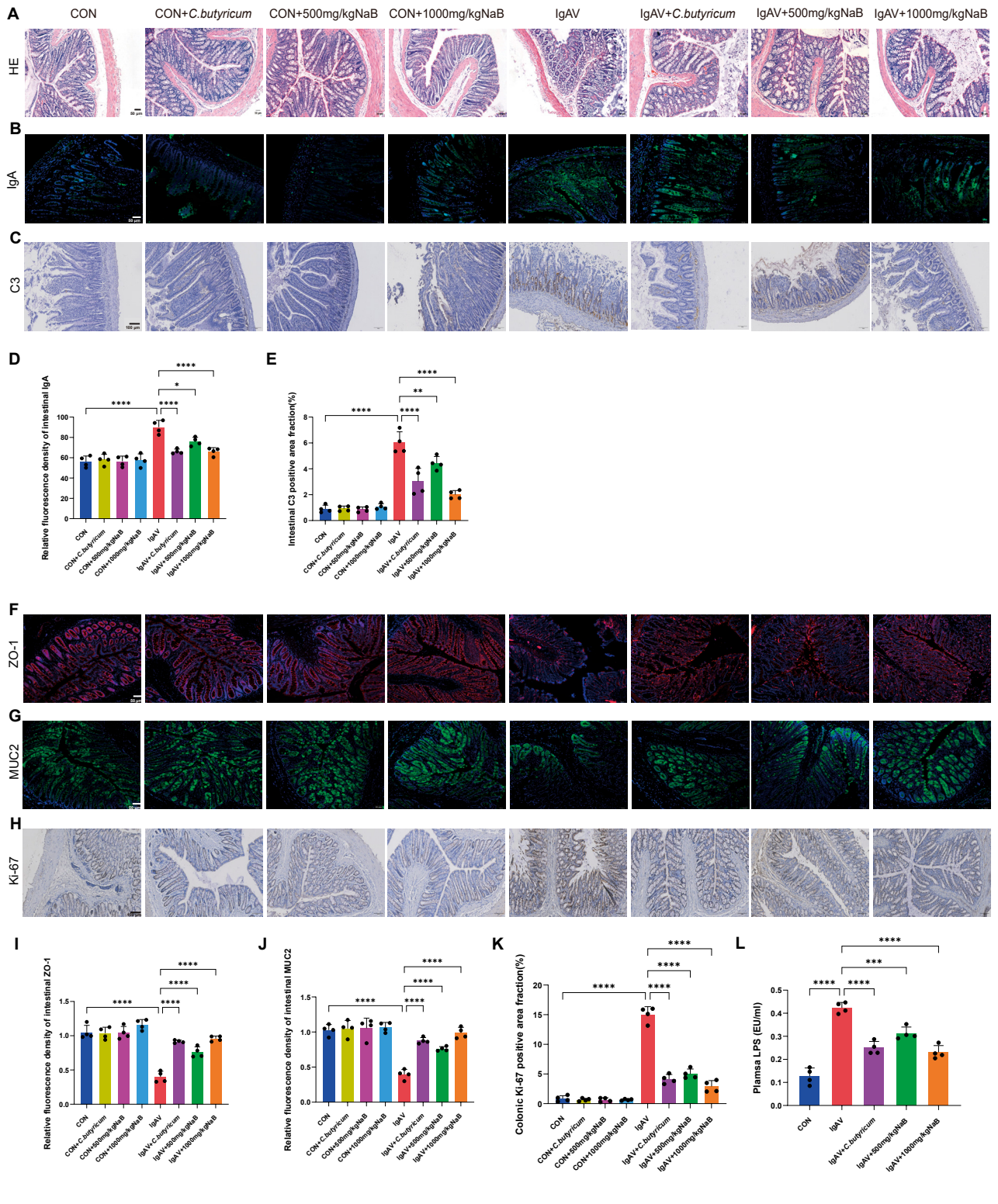

A
PCoA Plot
PC1 (19.51%)
PC2 (10.78%)
HC
IgAV
B
Alpha diversity difference
shannon
Hc
IgA
Group
group
HC
IgAV
C
venn2
HC
IgAV
1768167
1585246
1830778
D
Relative Abundance
HC
IgAV
Phylum
Others
p__Chloroflexota
p__Deinococcota
p__Spirochaetota
p__Ascomycota
p__Campylobacterota
p__Fusobacteriota
p__Hofneiviricota
p__Candidatus Melainabacteria
p__Synergistota
p__Chlamydiota
p__Mycoplasmatota
p__Candidatus Saccharibacteria
p__Euryarchaeota
p__Thermodesulfobacteriota
p__Uroviricota
p__Pseudomonadota
p__Verrucomicrobiota
p__Actinomycetota
p__Bacteroidota
p__Bacillota
E
Relative Abundance
HC
IgAV
Genus
Others
g__Parabacteroides
g__Collinsella
g__Blautia
g__Dialister
g__Segatella
g__Eubacterium
g__Clostridium
g__Streptococcus
g__Veillonella
g__Gemmiger
g__Phocaeicola
g__Roseburia
g__Megamonas
g__Bifidobacterium
g__Alistipes
g__Akkermansia
g__Agathobacter
g__Ruminococcus
g__Faecalibacterium
g__Bacteroides
F
Relative Abundance
HC
IgAV
Species
Others
s__Dialister invisus
s__[Ruminococcus] lactaris
s__Eubacterium sp. CAG:274
s__Phocaeicola coprocola
s__Faecalibacterium sp. CAG:74_58_120
s__Bifidobacterium adolescentis
s__Bacteroides fragilis
s__Segatella copri
s__Gemmiger formicilis
s__Firmicutes bacterium CAG:341
s__Bifidobacterium longum
s__Phocaeicola plebeius
s__Akkermansia muciniphila
s__Eubacterium sp. CAG:251
s__Roseburia intestinalis
s__Bifidobacterium pseudocatenulatum
s__Faecalibacterium prausnitzii
s__Agathobacter rectalis
s__Caudoviricetes sp.
s__Bacteriophage sp.
G
p__Bacillota
Relative Abundance
**
HC
IgAV
p__Bacteroidota
Relative Abundance
*
HC
IgAV
Bacillota/Bacteroidota ratio
*
HC
IgAV
H
g__Butyricicoccus
0.0261
g__Clostridium
0.0019
g__Eubacterium
0.0059
g__Roseburia
0.0128
g__Faecalibacterium
0.1361
HC
IgAV
I
s__Faecalibacillus faecis
0.0261
s__Coprococcus catus
0.0059
s__Roseburia hominis
0.0090
s__Roseburia intestinalis
0.0028
s__Agathobacter rectalis
0.0429
HC
IgAV

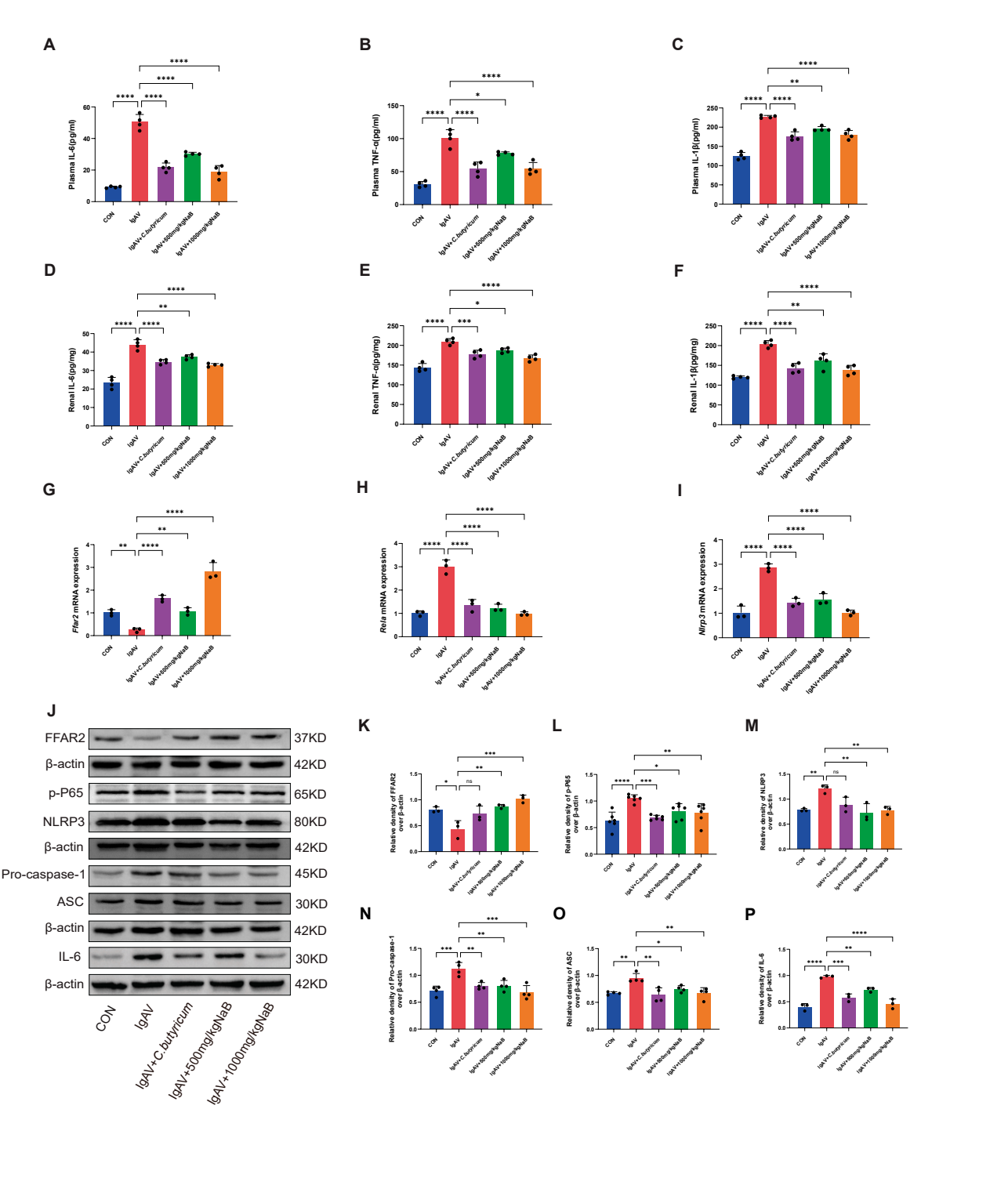

A
PCoA Plot
HC
IgAV
PC1 (43.3%)
PC2 (15.49%)
B
Relative Abundance
Names
type
Phosphotransferase system (PTS)
Pyruvate metabolism
Homologous recombination
Galactose metabolism
Aminoacyl-tRNA biosynthesis
Glycolysis / Gluconeogenesis
Cysteine and methionine metabolism
Pyrimidine metabolism
Amino sugar and nucleotide sugar metabolism
Starch and sucrose metabolism
Purine metabolism
Quorum sensing
Two-component system
Ribosome
ABC transporters
C
Butanoate metabolism
Glycerolipid metabolism
Starch and sucrose metabolism
0.1110
0.0261
0.0200
D
Butyrate-CoA transferase
Butyrate Kinase
0.0128
0.0773
E
AA(ug/g)
PA(ug/g)
BA(ug/g)
IBA(ug/g)
VA(ug/g)
IVA(ug/g)
CA(ug/g)
ns
F
24h UP (g/24h)
IgA(g/L)
IL-6(pg/mL)
CRP(mg/L)
ESR(mm/h)
FIB(g/L)
G
Non-renal IgAV
IgAVN
H
Spearman ρ=-0.3886
P=0.0549
Spearman ρ=-0.3464
P=0.0898
Spearman ρ=-0.3684
P=0.0700
I
Butanoate metabolism
Glycerolipid metabolism
Starch and sucrose metabolism
g__Faecalibacterium
g__Roseburia
g__Eubacterium
g__Clostridium
g__Butyricicoccus
J
24h UP
CRP
IL−6
IgA
g__Eubacterium
g__Clostridium
g__Butyricicoccus
g__Roseburia
g__Faecalibacterium

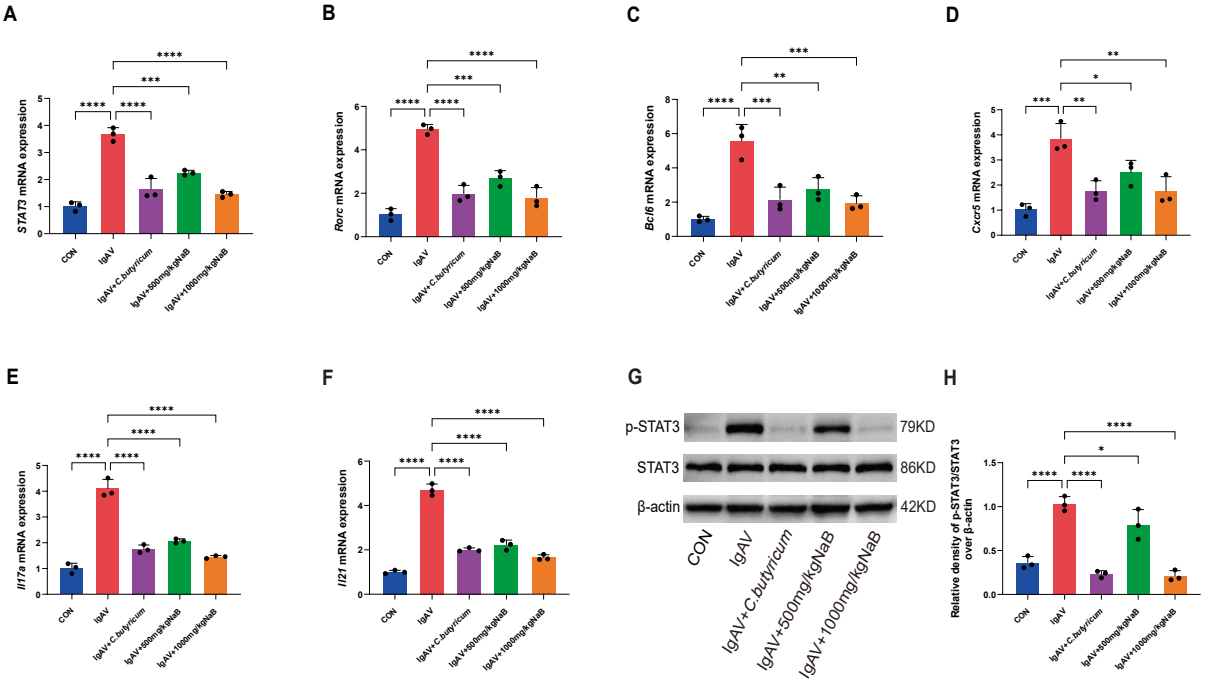

A
3-4w SD rats
Adaptation
1 week
OVA sensitized,10mg/kg,once a week,IP
3 Weeks
1%OVA,IV
0.3%OVA,ID
24h
Euthanized
B
Body weight (g)
Days
CON
CON+C.butyricum
CON+500mg/kgNaB
CON+1000mg/kgNaB
IgAV
IgAV+C.butyricum
IgAV+500mg/kgNaB
IgAV+1000mg/kgNaB
CON vs IgAV
IgAV vs IgAV+C.butyricum
IgAV vs IgAV+500mg/kgNaB
IgAV vs IgAV+1000mg/kgNaB
C
D
E
SCr
F
UUN
G
URBC
H
UTP
UCr
UPCR

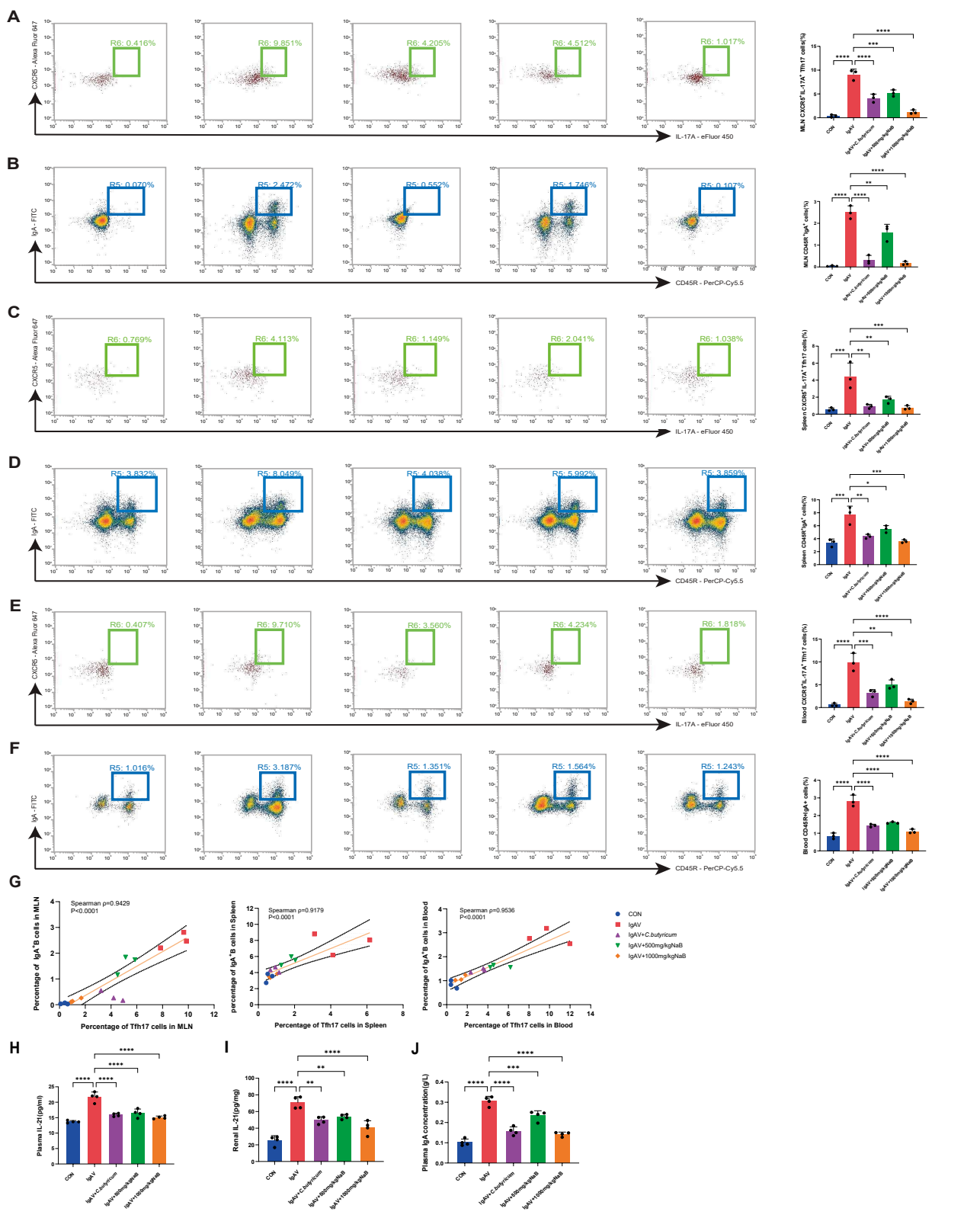

A
CON
CON+C.butyricum
CON+500mg/kgNaB
CON+1000mg/kgNaB
IgAV
IgAV+C.butyricum
IgAV+500mg/kgNaB
IgAV+1000mg/kgNaB
HE
B
IgA
C
C3
D
HE
E
PAS
F
IgA
G
C3

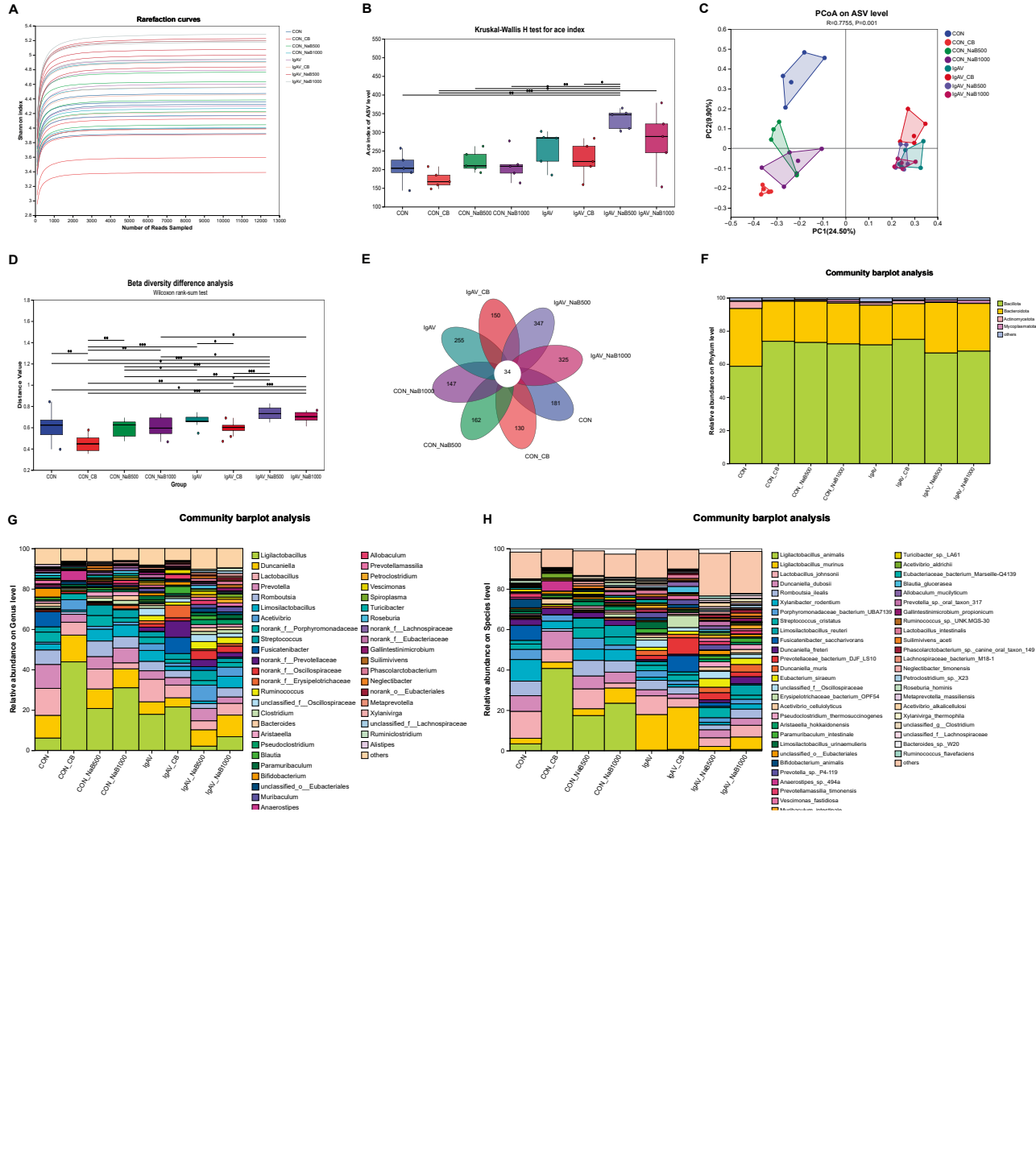

H
Relative fluorescence density of skin IgA
I
Skin C3 positive area fraction(%)
J
Relative fluorescence density of renal glomerular IgA
K
Glomerular C3 positive area fraction(%)
CON
CON+C.butyricum
CON+500mg/kgNaB
CON+1000mg/kgNaB
IgAV
IgAV+C.butyricum
IgAV+500mg/kgNaB
IgAV+1000mg/kgNaB

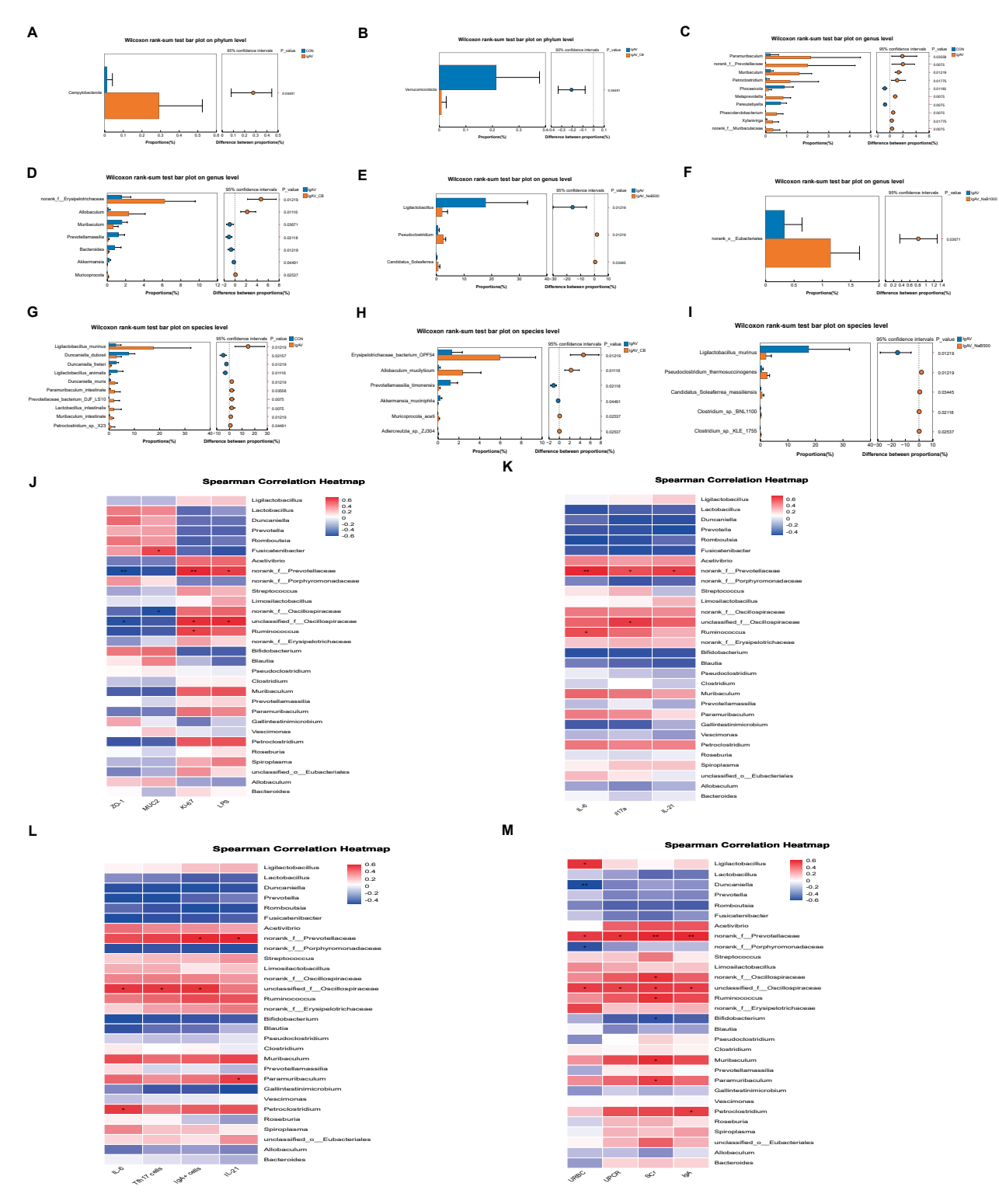

A
CON
CON+C.butyricum
CON+500mg/kgNaB
CON+1000mg/kgNaB
IgAV
IgAV+C.butyricum
IgAV+500mg/kgNaB
IgAV+1000mg/kgNaB
HE
B
IgA
C
C3
D
Relative fluorescence density of intestinal IgA
E
Intestinal C3 positive area fraction(%)
F
ZO-1
G
MUC2
H
Ki-67
I
Relative fluorescence density of intestinal ZO-1
J
Relative fluorescence density of intestinal MUC2
K
Colonic Ki-67 positive area fraction(%)
L
Plamsa LPS (EU/ml)

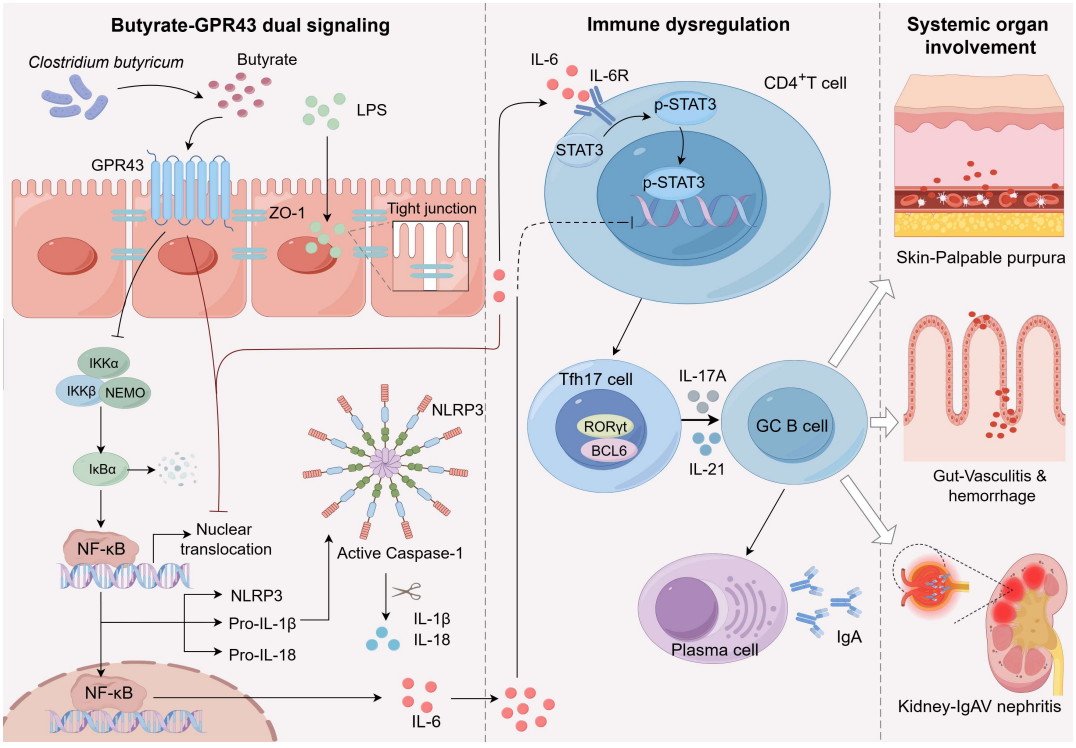

A
Plasma IL-6(pg/ml)
B
Plasma TNF-α(pg/ml)
C
Plasma IL-1β(pg/ml)
D
Renal IL-6(pg/mg)
E
Renal TNF-α(pg/mg)
F
Renal IL-1β(pg/mg)
G
Ffar2 mRNA expression
H
Rela mRNA expression
I
Nlrp3 mRNA expression
CON
IgAV
IgAV+C.butyricum
IgAV+500mg/kgNaB
IgAV+1000mg/kgNaB
J
FFAR2
β-actin
p-P65
NLRP3
β-actin
Pro-caspase-1
ASC
β-actin
IL-6
β-actin
37KD
42KD
65KD
80KD
42KD
45KD
30KD
42KD
30KD
42KD
K
Relative density of FFAR2 over β-actin
L
Relative density of p-P65 over β-actin
M
Relative density of NLRP3 over β-actin
N
Relative density of Pro-caspase-1 over β-actin
O
Relative density of ASC over β-actin
P
Relative density of IL-6 over β-actin


A
STAT3 mRNA expression
B
Rorc mRNA expression
C
Bcl6 mRNA expression
D
Cxcr5 mRNA expression
E
Il17a mRNA expression
F
Il21 mRNA expression
G
p-STAT3
STAT3
β-actin
79KD
86KD
42KD
H
Relative density of p-STAT3/STAT3 over β-actin
CON
IgAV
IgAV+C.butyricum
IgAV+500mg/kgNaB
IgAV+1000mg/kgNaB


A
R6: 0.416%
R6: 9.851%
R6: 4.205%
R6: 4.512%
R6: 1.017%
CXCR5 - Alexa Fluor 647
IL-17A - eFluor 450
MLN CXCR5+IL-17A+ Tfh17 cells(%)
B
R5: 0.070%
R5: 2.472%
R5: 0.552%
R5: 1.746%
R5: 0.107%
IgA - FITC
CD45R - PerCP-Cy5.5
MLN CD45R+IgA+ cells(%)
C
R6: 0.769%
R6: 4.113%
R6: 1.149%
R6: 2.041%
R6: 1.038%
Spleen CXCR5+IL-17A+ Tfh17 cells(%)
D
R5: 3.832%
R5: 8.049%
R5: 4.038%
R5: 5.992%
R5: 3.859%
Spleen CD45R+IgA+ cells(%)
E
R6: 0.407%
R6: 9.710%
R6: 3.560%
R6: 4.234%
R6: 1.818%
Blood CXCR5+IL-17A+ Tfh17 cells(%)
F
R5: 1.016%
R5: 3.187%
R5: 1.351%
R5: 1.564%
R5: 1.243%
Blood CD45R+IgA+ cells(%)
CON
IgAV
IgAV+C.butyricum
IgAV+500mg/kgNaB
IgAV+1000mg/kgNaB
G
Spearman ρ=0.9429
P<0.0001
Percentage of IgA+B cells in MLN
Percentage of Tfh17 cells in MLN
Spearman ρ=0.9179
P<0.0001
percentage of IgA+B cells in Spleen
Percentage of Tfh17 cells in Spleen
Spearman ρ=0.9536
P<0.0001
Percentage of IgA+B cells in Blood
Percentage of Tfh17 cells in Blood
H
Plasma IL-21(pg/ml)
I
Renal IL-21(pg/mg)
J
Plasma IgA concentration(g/L)


A
Rarefaction curves
Shannon index
Number of Reads Sampled
CON
CON_CB
CON_NaB500
CON_NaB1000
IgAV
IgAV_CB
IgAV_NaB500
IgAV_NaB1000
B
Kruskal-Wallis H test for ace index
Ace index of ASV level
C
PCoA on ASV level
R=0.7755, P=0.001
PC2(9.90%)
PC1(24.50%)
D
Beta diversity difference analysis
Wilcoxon rank-sum test
Distance Value
Group
E
150
347
325
255
147
34
181
162
130
F
Community barplot analysis
Relative abundance on Phylum level
Bacillota
Bacteroidota
Actinomycetota
Mycoplasmatota
others
G
Community barplot analysis
Relative abundance on Genus level
Ligilactobacillus
Duncaniella
Lactobacillus
Prevotella
Romboutsia
Limosilactobacillus
Acetivibrio
norank_f__Porphyromonadaceae
Streptococcus
Fusicatenibacter
norank_f__Prevotellaceae
norank_f__Oscillospiraceae
norank_f__Erysipelotrichaceae
Ruminococcus
unclassified_f__Oscillospiraceae
Clostridium
Bacteroides
Aristaeella
Pseudoclostridium
Blautia
Paramuribaculum
Bifidobacterium
unclassified_o__Eubacteriales
Muribaculum
Anaerostipes
Allobaculum
Prevotellamassilia
Petroclostridium
Vescimonas
Spiroplasma
Turicibacter
Roseburia
norank_f__Lachnospiraceae
norank_f__Eubacteriaceae
Gallintestinimicrobium
Suilimivens
Phascolarctobacterium
Neglectibacter
norank_o__Eubacteriales
Metaprevotella
Xylanivirga
unclassified_f__Lachnospiraceae
Ruminiclostridium
Alistipes
others
H
Community barplot analysis
Relative abundance on Species level
Ligilactobacillus_animalis
Ligilactobacillus_murinus
Lactobacillus_johnsonii
Duncaniella_dubosii
Romboutsia_ilealis
Xylanibacter_rodentium
Porphyromonadaceae_bacterium_UBA7139
Streptococcus_cristatus
Limosilactobacillus_reuteri
Fusicatenibacter_saccharivorans
Duncaniella_freteri
Prevotellaceae_bacterium_DJF_LS10
Duncaniella_muris
Eubacterium_siraeum
unclassified_f__Oscillospiraceae
Erysipelotrichaceae_bacterium_OPF54
Acetivibrio_cellulolyticus
Pseudoclostridium_thermosuccinogenes
Aristaeella_hokkaidonensis
Paramuribaculum_intestinale
Limosilactobacillus_urinaemulieris
unclassified_o__Eubacteriales
Bifidobacterium_animalis
Prevotella_sp._P4-119
Anaerostipes_sp._494a
Prevotellamassilia_timonensis
Vescimonas_fastidiosa
Turicibacter_sp._LA61
Acetivibrio_aldrichii
Eubacteriaceae_bacterium_Marseille-Q4139
Blautia_glucerasea
Allobaculum_mucilyticum
Prevotella_sp._oral_taxon_317
Gallintestinimicrobium_propionicum
Ruminococcus_sp._UNK.MGS-30
Lactobacillus_intestinalis
Suilimivens_aceti
Phascolarctobacterium_sp._canine_oral_taxon_149
Lachnospiraceae_bacterium_M18-1
Neglectibacter_timonensis
Petroclostridium_sp._X23
Roseburia_hominis
Metaprevotella_massiliensis
Acetivibrio_alkalicellulosi
Xylanivirga_thermophila
unclassified_g__Clostridium
unclassified_f__Lachnospiraceae
Bacteroides_sp._W20
Ruminococcus_flavefaciens
others


A
Wilcoxon rank-sum test bar plot on phylum level
Campylobacteria
Proportions(%)
Difference between proportions(%)
B
Wilcoxon rank-sum test bar plot on phylum level
Verrucomicrobiota
C
Wilcoxon rank-sum test bar plot on genus level
Paramuribaculum
norank_f__Prevotellaceae
Muribaculum
Petroclostridium
Phocaeicola
Metaprevotella
Pseudobutyrivibrio
Phascolarctobacterium
Xylanivirga
norank_f__Muribaculaceae
D
Wilcoxon rank-sum test bar plot on genus level
norank_f__Erysipelotrichaceae
Allobaculum
Muribaculum
Prevotellamassilia
Bacteroides
Akkermansia
Muricoprocola
E
Wilcoxon rank-sum test bar plot on genus level
Ligilactobacillus
Pseudoclostridium
Candidatus_Soleaferrea
F
Wilcoxon rank-sum test bar plot on genus level
norank_o__Eubacteriales
G
Wilcoxon rank-sum test bar plot on species level
Ligilactobacillus_murinus
Duncaniella_dubosii
Duncaniella_freteri
Ligilactobacillus_animalis
Duncaniella_muris
Paramuribaculum_intestinale
Prevotellaceae_bacterium_DJF_LS10
Lactobacillus_intestinalis
Muribaculum_intestinale
Petroclostridium_sp._X23
H
Wilcoxon rank-sum test bar plot on species level
Erysipelotrichaceae_bacterium_OPF54
Allobaculum_mucilyticum
Prevotellamassilia_timonensis
Akkermansia_muciniphila
Muricoprocola_aceti
Adlercreutzia_sp._ZJ304
I
Wilcoxon rank-sum test bar plot on species level
Ligilactobacillus_murinus
Pseudoclostridium_thermosuccinogenes
Candidatus_Soleaferrea_massiliensis
Clostridium_sp._BNL1100
Clostridium_sp._KLE_1755
J
Spearman Correlation Heatmap
Ligilactobacillus
Lactobacillus
Duncaniella
Prevotella
Romboutsia
Fusicatenibacter
Acetivibrio
norank_f__Prevotellaceae
norank_f__Porphyromonadaceae
Streptococcus
Limosilactobacillus
norank_f__Oscillospiraceae
unclassified_f__Oscillospiraceae
Ruminococcus
norank_f__Erysipelotrichaceae
Bifidobacterium
Blautia
Pseudoclostridium
Clostridium
Muribaculum
Prevotellamassilia
Paramuribaculum
Gallintestinimicrobium
Vescimonas
Petroclostridium
Roseburia
Spiroplasma
unclassified_o__Eubacteriales
Allobaculum
Bacteroides
ZO-1
MUC2
Ki-67
LPS
K
Spearman Correlation Heatmap
IL-6
IL17a
IL-21
L
Spearman Correlation Heatmap
IL-6
Th17 cells
IgA+ cells
IL-21
M
Spearman Correlation Heatmap
URSC
UPCR
SCT
IgA


Butyrate-GPR43 dual signaling
Immune dysregulation
Systemic organ involvement
Clostridium butyricum
Butyrate
LPS
GPR43
ZO-1
Tight junction
IKKα
IKKβ
NEMO
IκBα
NF-κB
Nuclear translocation
NLRP3
Pro-IL-1β
Pro-IL-18
Active Caspase-1
IL-1β
IL-18
NF-κB
IL-6
IL-6
IL-6R
CD4+T cell
p-STAT3
STAT3
p-STAT3
Tfh17 cell
RORγt
BCL6
IL-17A
IL-21
GC B cell
Plasma cell
IgA
Skin-Palpable purpura
Gut-Vasculitis & hemorrhage
Kidney-IgAV nephritis

Supplementary Files

This is a list of supplementary files associated with this preprint. Click to download.

- Supplement.docx
- UncroppedWB.doc
- figureS1.pdf
- figures2.pdf